ORNL-6955

ornl

![OAK RIDGE NATIONAL LABORATORY LOCKHEED MARTIN]

OAK RIDGE NATIONAL LABORATORY

LOCKHEED MARTIN

RECEIVED
NOV 02 1999
OSTI

On the Mechanical Response of Chopped Glass/Urethane Resin Composite: Data and Model

M. Elahi
Y. J. Weitsman

DISCLAIMER

Portions of this document may be illegible in electronic image products. Images are produced from the best available original document.
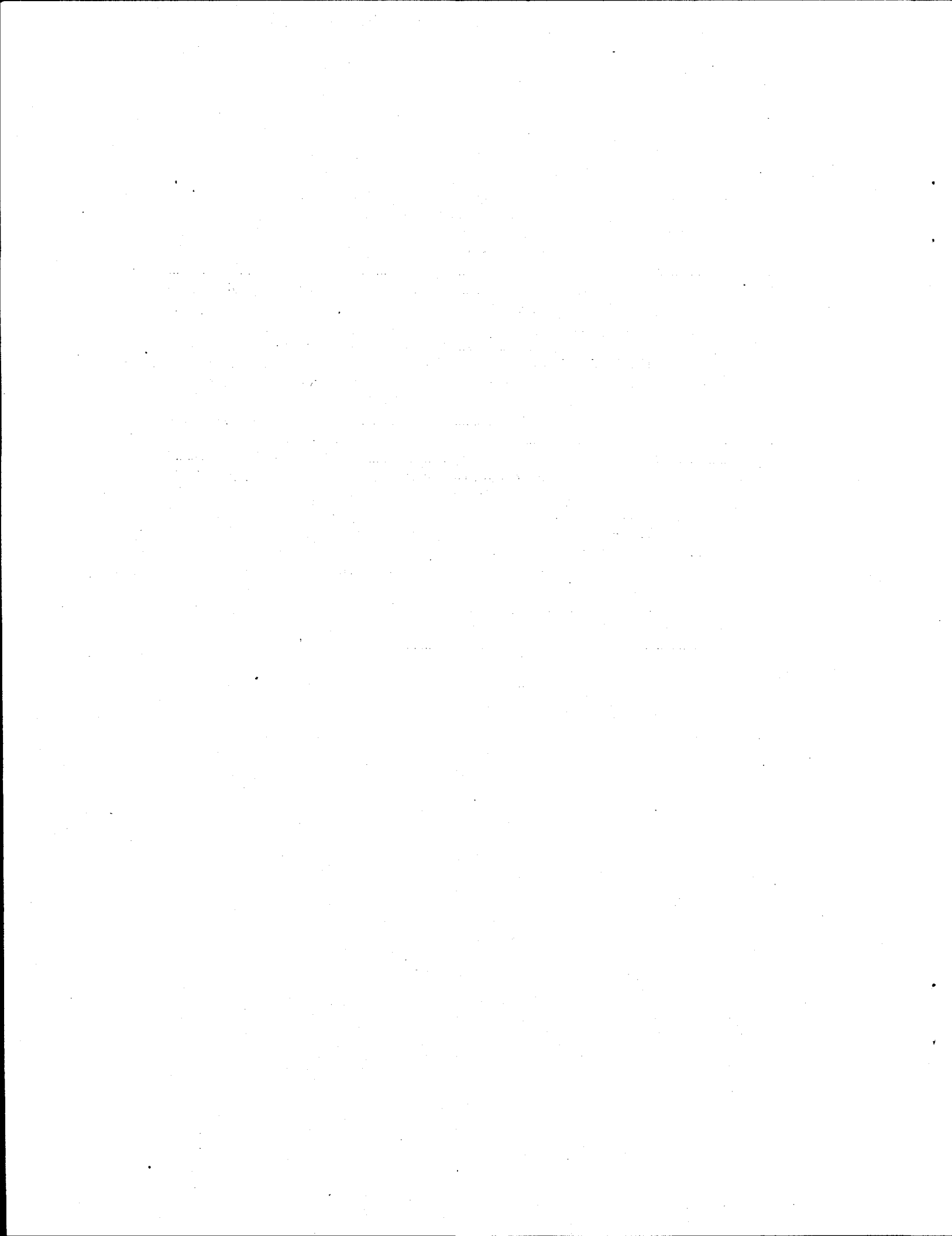
Engineering Technology Division

ON THE MECHANICAL RESPONSE OF P4 CHOPPED GLASS/URETHANE RESIN COMPOSITE: DATA AND MODEL

M. Elahi and Y. J. Weitsman

October 1999

CONTENTS

LIST OF FIGURES

LIST OF TABLES

PREFACE

This report presents a portion of a larger investigation undertaken at Oak Ridge National Laboratory (ORNL) on the durability of polymeric composites for automotive structural applications. The ORNL project, which is entitled "Durability of Lightweight Composite Structures for Automotive Applications," is sponsored by the U.S. Department of Energy Office of Advanced Automotive Technologies.

The main purpose of this report is to demonstrate the applicability of a theoretically based methodology to model and predict the response of a class of randomly reinforced polymeric composites under consideration for automotive applications. Theoretical modeling and experimental investigations progressed interactively throughout this investigation, demonstrating the essential need for the systemic establishment of a comprehensive database conjointly with theory.

While this report is aimed towards the mechanics and materials community, several practical implications that may be useful to designers as well are listed in the conclusion section.

ON THE MECHANICAL RESPONSE OF P4 CHOPPED GLASS/URETHANE RESIN COMPOSITE SYSTEM: DATA AND MODEL

M. Elahi* and Y. J. Weitsman*

ABSTRACT

This report presents data on the creep response of a polymeric composite that is a candidate material for automotive applications. The above data were used to establish the basis for the mechanical characterization of the material's response over a wide range of stresses and temperatures, as well as under cyclic loading and due to exposure to distilled water.

A constitutive model based upon fundamental principles of irreversible thermodynamics and continuum mechanics was employed to encompass the abovementioned database and to predict the response under more complex inputs. These latter tests verified the validity of the model.

1. INTRODUCTION

This report concerns the mechanical response of P4 chopped glass/urethane resin composites under a wide range of stresses and temperatures as well as under exposure to distilled water. Attention is confined to the case of uniaxial tensile stresses, both static and cyclic.

The chopped-mat composites consist of a fiber preform and a polymeric matrix, which acts a binder. This preform is produced by depositing 5 cm long chopped glass fiber strands (Owens Corning chopped E-glass fibers produced specifically for the P4 process) in a random pattern deposited on a screen. The fiber strands are held in place by airflow. To preserve the shape and enhance the wettability during the structural reaction injection molding (SRIM), a powdered thermoplastic binder is blown into the chopped mat. Subsequently, hot air is blown into the mat to melt the binder, followed by a stream of cold air to set the binder. The glass preform is then loaded into a mold of a prescribed shape where the Bayer 420 IMR resin (a urethane polymer with internal mold release) is injected into the preform at high pressure. After 4 minutes the part is taken out and is post cured at 121 °C for 1 hour. The composite has a fiber volume fraction of V_f=29.6% (47.3% by weight), a modulus of E=12.9 GPa, tensile strength of σ_{ult}=193 MPa, failure strain of ε_f=1.94%, Poison's ratio of v=0.336, and coefficient of linear thermal expansion of α=18.1 $\mu\varepsilon$/°C.

Experiments were performed on flat coupons, typically measuring 20 cm by 2.5 cm in length and width and of 3 mm in thickness. All mechanical data were collected on an MTS hydraulic testing machine under load control, with strains recorded by means of strain gages and extensometry.

The abovementioned composite exhibits a wide scatter in its basic properties, such as stiffness, strength and strain-to-failure. Its mechanical response incorporates features attributable to viscoelastic creep coupled with distributed damage. In all the foregoing respects the response of this composite is analogous to that of a previously investigated swirl-mat material [1-3].

Consequently, it was possible to characterize the response of the composite at hand on the basis of an experimental program and a theoretical model similar to those established earlier [1-5].

The usefulness of the model presented herein is validated by comparing model predictions against experimentally recorded responses to stress and temperature inputs, as well as input durations, which differed from those employed in the experimental characterization program.

2. CREEP RESPONSE

The creep response of the composite was characterized experimentally by collecting short-term creep and recovery strain data associated with the application of a step load of magnitude σ_o and its removal after time t_o. In all characterization tests $t_o = 30$ min, with recovery strains recorded for an additional duration $t_r \geq 3t_o$.

---

*MAES Department, University of Tennessee, Knoxville, TN 37996-2030 and Engineering Technology Division, Oak Ridge National Laboratory, M/S 8051, Oak Ridge, TN 37830-8051.

The response was deemed to be linear when it satisfied the two following conditions: (i) strain was proportional to stress, and (ii) strain was completely recovered after a sufficiently long recovery time.

A schematic representation of the characterization scheme is shown in Fig. 1, with stress input given in Fig. 1(a), and the recorded strain output sketched in Fig. 1(b). In the latter figure ε_p denotes unrecoverable, permanent strain, as encountered when $\sigma \geq \sigma_d$.

The above mentioned experiments were performed at five levels of σ_o at three distinct temperatures T, with at least three replicate tests for each pair of values (σ_o, T). A listing of the experimental program is given in Table 1.

Table 1. Test program for short-term creep and recovery of P4 chopped glass/urethane composite

σ_{max} MPa (ksi)	Test temperature °C (°F)	Creep time t_o (min)	Recovery time (min)	No. of tests per temp. per stress
25 (3.63)	23,50,120 (73,122,248)	30	$\geq 3t_o$	≥ 3
50 (7.25)	23,50,120 (73,122,248)	30	$\geq 10t_o$	≥ 3
75 (10.9)	23,50,120 (73,122,248)	30	$\geq 10t_o$	≥ 3
100 (14.5)	23,50,120 (73,122,248)	30	$\geq 10t_o$	≥ 3
125 (18.1)	23,50,120 (73,122,248)	30	$\geq 10t_o$	≥ 3

2.1 ROOM-TEMPERATURE RESPONSE: DATA AND MODEL

It was observed that at $T = 23$ °C the range of linear response was confined to $0 \leq \sigma \leq \sigma_d = 40$ MPa. Furthermore, it was possible to express the creep response in a power-law form as follows

$$\varepsilon(t) = \begin{cases} (D_o + D_1 t^n)\sigma_o & 0 \leq t \leq t_o \\ D_1[t^n - (t - t_o)^n]\sigma_o & t \geq t_o \end{cases} \qquad (1)$$

In Eqs. (1), $\sigma_o \leq \sigma_d$ and the response parameters are $7.39 \times 10^{-5} < D_o < 8.16 \times 10^{-5}$ MPa^{-1}, $7.24 \times 10^{-6} < D_1 < 12.7 \times 10^{-6}$ MPa^{-1} min^{-n}, $n = 0.086$ and time t is in minutes.

Note the wide spread in the values of D_o and D_1, which reflects the sample-to-sample variability attributed to material inhomogeneity and processing non-uniformity. This wide scatter in material properties can easily mask the effects of the parameters, such as stress, temperature and moisture that govern the material's response, thereby reducing any modeling effort to a futile exercise. Consequently, it was necessary to scale *all* deformation data collected in the experimental tasks presented in this report by the ratio of the specimen's stiffness to a common reference stiffness in order to account for sample-to-sample variability. The reference stiffness was selected as the average of all values recorded in the experimental program. The abovementioned scaling substantially reduced the data scatter (typically a four-fold reduction). The foregoing inhomogeneity was detectable even *within* an individual coupon, which can be seen from the distinct, simultaneously recorded, creep curves by strain gages located at five distinct positions over a coupon's length, as shown in Fig. 2.

It is also worth noting that while three parameters, D_o and D_1, and n are employed in Eq. (1) to express creep, employment of the Boltzman superposition integral to relate viscoelastic strain-stress response, namely

$$\varepsilon(t) = \int_0^t D(t-\tau) \, \frac{d\sigma(\tau)}{d\tau} \, d\tau \tag{2}$$

yields an expression for the recovery strain that contains only two of the above parameters. Consequently, it is more convenient to first evaluate D_1, and n from recovery data and subsequently determine D_o from creep data. Typical creep and recovery data and their power-law representation are shown in Fig. 3.

Turning to the nonlinear range of creep response, involving the four stresses that exceed $40\,MPa$ listed in Table 1, it was necessary to first evaluate the creep and recovery responses of each individual coupon in the linear range ($\sigma_o = 25\,MPa$ and $t_o = 30$ min) to establish its so called "reference signature". This enabled the appropriate scaling of subsequent deformation data, thereby accounting for sample-to-sample variability. As noted earlier, this procedure has significantly reduced the data scatter. Results are shown in Fig. 4. Although, these results exhibit a fairly small degree of nonlinearity, it is possible to discern the presence of nonlinear response in the data for the permanent residual strain ε_p vs. σ shown in Fig. 5. Equivalently, these data can be related to the maximum strain attained by the material while subjected to loading, as can be seen in Fig. 6. Figures 5 and 6 contain empirical expressions for ε_p.

. Guided by previous investigations [1-3], it is reasonable to attribute the aforementioned nonlinearity to the stress induced onset of profuse microcracking within the composite. As before, permanent deformation is ascribed to the roughness and geometric mismatches that arise over opposing micro-crack surfaces, which prevent their complete closure upon load removal.

It was possible to correlate the data shown in Fig. 4 by means of two scaled, stress dependent functions $D_o(\sigma)$ and $D_1(\sigma)$ shown in Figs. 7 and 8. The figures shown contain the curve-fitted, empirical expressions for the above terms. Note that $n = 0.086$, remaining unchanged from the linear range. Consequently, one obtains for $\sigma_o > \sigma_d = 40\,MPa$

$$\varepsilon(t) = \begin{cases} [D_o(\sigma_o) + D_1(\sigma_o)t^n]\sigma_o & 0 < t < t_o \\ D_1(\sigma_o)[t^n - (t-t_o)^n]\sigma_o + \varepsilon_p. & t > t_o \end{cases} \tag{3}$$

While $D_o(\sigma)$ and $D_1(\sigma)$ relate the effect of stress-enhanced profuse micro-cracking("damage") on compliance, these expressions do not account for time-dependent damage growth. Thereby, Eqs. (3) remain valid for sufficiently short load durations $t_o \ll t_f$, where t_f denotes failure time.

The predictive capability of the model, as expressed in Eqs. (1) and (3), was tested by performing two-stage loading experiments. In one case a coupon was first subjected to a step load $\sigma_1 = 100\,MPa$ for a duration $t_o = 30$ min, then allowed to recover. In view of the results shown in Fig. 5 the above loading resulted in a permanent strain of $\varepsilon_p \sim 200\,\mu$.

Subsequently, the coupon was subjected to a second step loading $\sigma_2 = 75\,MPa$. By hypothesis, no new damage occurs under $\sigma_2 < \sigma_1$; thereby deformation should now be simply scaled by a factor of $\sigma_2 / \sigma_1 = 0.75$. Results, together with the foregoing prediction, are shown in Fig. 9.

Note that Fig. 9 exhibits two sets of predictions. One prediction is based upon the average values of $D_o(\sigma)$ and $D_1(\sigma)$ that correspond to the expressions incorporated in Figs. 7 and 8, while the other prediction is based upon the values of $D_o(\sigma)$ and $D_1(\sigma)$ that provide the best power-law fit for the strain due to σ_1, which are specific to the coupon at hand. It is worthwhile to note that the actual strains under σ_2 in Fig. 9 are proportional to those under σ_1 by a factor of 0.74 (As compared with the theoretical ratio of 0.75).

The second verification test involved a similar two-stage loading experiment, except that now $\sigma_2 > \sigma_1$. In this case, the strain under σ_2 is given by

$$\varepsilon(t) = [D_o(\sigma_2) + D_1(\sigma_2)t^n]\sigma_2 + \varepsilon_p(\sigma_1) \quad . \tag{4}$$

Comparative results are shown in Fig. 10.

2.2 ELEVATED TEMPERATURE RESPONSE: DATA AND MODEL

The elevated temperature characterization scheme was based upon creep and recovery data and followed the test program listed in Table 1. As noted therein, the elevated temperatures were $50\,^oC$ and $120\,^oC$.

All elevated temperature tests were preceded by room-temperature experiments that characterized the response of each coupon within the linear range ($\sigma = 25\ MPa$) and subsequently at the specific stress level ($\sigma = 50, 75, 100$, or $125\ MPa$) under consideration. The purpose of room temperature pre-testing in the linear range was to account for, and thereby reduce, the effect of sample-to-sample variability, while the aim of room-temperature testing at the corresponding stress-level within the nonlinear range of response was to separate the effects of stress from those of temperature.

Results, including data scatter, are shown in Figs. 11 and 12. The data scatter remains after scaling, which accounted for sample-to-sample stiffness variability. Note the pronounced nonlinearity in strain in relation to stress exhibited in Figs. 11 and 12. The nonlinearity increases with temperature. All samples tested at $\sigma = 125\ MPa$ and $T = 120\ ^oC$ failed within about three minutes.

It was possible to represent the data in Figs. 4, 11, and 12 in the standard format which, together with the power-law expression (1), reads

$$\varepsilon(t;\sigma;T) = \left\{ \hat{D}_o(\sigma;T) + D_1(\sigma)[t / a_T(T)]^n \right\} \sigma + \alpha \Delta T \tag{5}$$

where α denotes the coefficient of thermal expansion and $\Delta T = T - T_{reference}$.

It turned out that it was possible to express $\hat{D}_o(\sigma;T)$ in product form, namely $\hat{D}_o(\sigma;T) = D_o(\sigma)F(T)$. Values of $F(T)$ and the "shift-factor" $a_T(T)$ are drawn against T in Figs. 13 and 14. These figures also contain the "best fit" empirical expressions.

Experimental verification of the predictive ability of Eq. (5) was based on two types of tests. In the first case the application and removal of a step load was accompanied by a documented temperature history, as shown in Fig. 15. Specific values of D_o and D_1, for the sample at hand were obtained from a prior test at room temperature. In this case Eq. (5) reads

$$\varepsilon(t;T) = \left\{ D_o F(T) + D_1 \xi(t)^n \right\} \sigma + \alpha \Delta T \tag{5a}$$

where

$$\xi(t) = \int_o^t du / a_T[T(u)] \quad . \tag{5b}$$

Predictions based upon Eq. (5a) are compared against data in Fig. 15, with $\alpha = 18\ \mu\varepsilon/^oC$ and $T_{reference} = 25\ ^oC$. This figure contains also the comparative linear thermoelastic predictions.

The second validation derives from the extension of model predictions, which are based on short-term (30-min.) data, whereby $t \ll t_f$, into the time domain, and comparing them with long-term creep data.[*] Results, at several levels of stress and temperature are shown in Fig. 16. These include predicted scatter bands due to material variability. Note the remarkable agreements with all long-term data.

3. SOME OBSERVATIONS REGARDING CREEP RUPTURE AND DAMAGE GROWTH

While creep rupture *per se* falls outside the scope of this investigation,[†] detailed data were collected from multiply-gaged samples in order to explore some features of damage growth in the composite considered herein.

The experiment utilized two 29 cm.-long coupons, with strains recorded at seven equally spaced locations over its length, with an additional strain recorded by means of an extensometer. Values of Poisson's ratio were recorded within the linear range at the seven foregoing locations for one of the coupons. Results for specimen no. 2 are shown in Fig. 17 and listed in Table 2. Figure 17 includes a listing of the initial stiffnesses under each of the seven gages and the extensometer, with accompanying numbers indicating ordered gage positions starting from the top. Note the wide spread in strain data, which is consistent with Fig. 2. More significantly,

---

[*] These data were collected on creep load frames by W. Ren at ORNL.

[†] Ongoing creep-rupture experiments are being performed elsewhere at ORNL under this project.

4

Table 2. Material properties measured along two 29 cm-long coupons

Strain gage number	Specimen no. 1 Stiffness, E (GPa)	Specimen no. 1 Poison's ratio, ν	Specimen no. 2 Stiffness, E (GPa)
1	10.69	0.30	9.86
2	12.30	0.35	9.79
3	11.99	0.39	9.24^b
4	12.11 (12.89^a)	0.40	10.41 (11.31^a)
5	11.68	0.37	11.31
6	10.11^b	0.36	12.00
7	11.99	0.31	11.10
Average	11.53	0.35	10.53

^{a}Extensometer was used.
^{b}Indicates failure location.

the location of failure is associated with the position of lowest stiffness, with localization ranging within approximately two centimeters about the failed cross section. It can also be seen that strain rises sharply with time prior to failure at $t = t_f = 2041$ min. Local values of cross-sectional areas were considered in all multigaged coupons.

Focusing attention on the strain recorded at the failed location, it was attempted to relate its time dependence to growing damage, in addition to the effect of stress. As a first step the above strain was related by means of the power-law given in Eq. (3), which should well fit the short-time data*. A very good fit, up to $t^* = 1000$ min., was indeed established by utilizing $D_o(\sigma) = 1.19 \times 10^{-4}$ MPa^{-1}, $D_1(\sigma) = 2.00 \times 10^{-5}$ MPa^{-1} min^{-n} and $n = 0.086$. Beyond t^* creep data exceeded values predicted by the power expression, by the amount shown in Fig. 18 and, in an expanded view, in Fig. 19. The excessive strain was attributed to damage growth.

Let $g(t)$ denote the time-dependent portion of damage growth. Thus, for $0 < t < t_f$ one has[4]

$$\varepsilon(t;\sigma,g(t))/\sigma = D_o(\sigma) + D_1(\sigma)t^n + D_o(\sigma)g(t) + D_1(\sigma)\int_0^t (t-\tau)^n g'(\tau)d\tau \qquad (6)$$

where $g(0) = 0$.

The last two terms on the right hand side of Eq. (6) should account for the excessive strain shown in Fig. 19.

Inspection of Fig. 19 suggests that $g(t)$ should contain a combination of slowly varying and rapidly varying functions of time. This motivates the following representation

$$g(t) = \hat{A}t^p + \hat{B}t^q \qquad (7)$$

with $q \gg p$.

Substitution of Eq. (7) into the last two terms on the right side of Eq. (6) yields, after some manipulations[†]

---

*Recall that Eq. (3) reflects the experimental observation that *for short times* D_o and D_1 do not depend on load duration.
[†]These manipulations include a two terms Taylor series expansion of $\Gamma(p+n)$ about $\Gamma(p)$ and similarly for $\Gamma(q+n)$.

$$D_o(\sigma)g(t) + D_1(\sigma)\int_o^t (t-\tau)^n g'(\tau)d\tau \cong D_o(\sigma)\left[A\left(\frac{t}{t_f}\right)^p + B\left(\frac{t}{t_f}\right)^q\right] +$$

$$D_1(\sigma)t_f^n\left[A\frac{\Gamma(n+1)}{1+n\Psi(p+1)}\left(\frac{t}{t_f}\right)^{n+p} + B\frac{\Gamma(n+1)}{1+n\Psi(q+1)}\left(\frac{t}{t_f}\right)^{n+q}\right]. \qquad (8)$$

In Eq. (8) Γ and Ψ denote the Gamma and Digamma functions, respectively.

A reasonable data fit for the effect of time dependent damage growth was achieved by selecting $p = 4$ and $q = 75$, $A = 0.5752$ and $B = 3.1825$. Results are shown in Figs. 18 and 19.

The latter figures suggest that the deformation of the composite at hand involves three distinct processes. For times up to approximately $t_f/2$ stress-induced damage, probably in the form of interfacial fiber/matrix microcracks remains fixed. Thus at earlier times all creep is due to molecular-level motions within the polymeric phase. This creep is modeled very accurately by Eq. (3). Subsequently, geometric changes due to the growth of the micro-cracks contribute to the overall deformation of the composite. This effect is reflected through the lower power p in Eq. (8).

Finally, the fibers themselves unravel within the strands and break. This last stage, which develops very rapidly and leads to failure, is modeled by the high exponent q in Eq. (8).

It is interesting to note that traces of the phenomenon shown in Fig. 18 are recorded by the neighboring gages (#2 and #4), which straddle the failed cross-section. These are shown in Figs. 20, 21, and 22. Note, however, the substantial diminutions in the amplitudes of the strain increments near failure, when compared to the data shown in Figs. 18 and 19. It is furthermore worth noting that at those neighboring locations, strains are predicted by the power-law expression (3) for times nearly up to failure. Consequently, it is possible to conclude that failure is localized within a region of approximately two centimeters about the failed cross-section.

4. SOME ASPECTS OF THE RESPONSE OF URETHANE RESIN

Exploratory tests were performed to evaluate the stress-strain and creep response of the "neat" resin. Stress-strain to failure results are shown in Fig. 23, with material properties, as reduced from that figure, listed in Table 3. Note the general agreement between results derived from two different samples, in contrast with the consistent disparity between strain gage and extensometer readings. A possible explanation for that disparity is that it stems from the unequal lengths of the strain gage (1.25 cm) and extensometer (2.5 cm). Whereby these two devices record distinct average values. It appears that linearity persists up to about $\sigma = 10$ MPa.

Creep and recovery data are shown in Figs. 24 and 25 respectively, for $\sigma = 25$ MPa. Note the residual permanent strain that persists in the recovery range. Typical data for the composite are shown in Figs. 24 and 25 for comparison.

Table 3. Tensile test results of urethane (neat resin) specimens

Specimen no.		E (GPa)	σ_{ult} (MPa)	ε_f ($\mu\varepsilon$)	ν	t_f (sec)
E-1	Strain gage	4.35	64.64	16806	0.33	21
E-1	Extensometer	3.50	64.64	22085		
E-2	Strain gage	4.59	58.19	14039	0.36	17
E-2	Extensometer	3.47	58.19	19145		
Average	Strain gage	4.47	61.42	15423	0.34	19
Average	Extensometer	3.49	61.42	20615		

5. CYCLIC BEHAVIOR

The cyclic tensile behavior of the composite was investigated under a "saw-tooth" stress input by recording the resulting strain response. These are shown schematically in Fig. 26.

The test plan involved the imposition of four levels of σ_{max}, each with three corresponding levels of σ_{min}(or $R = \sigma_{min}/\sigma_{max}$). Cycling was done at a frequency of 1 *Hz* and continued up to 2000 *cycles*. Three replicate specimens were used at each pair of values (σ_{max}, R). The details are given in Table 4. All strains were recorded by means of extensometry.

Table 4. Test program for short-term cyclic fatigue of P4 chopped glass/urethane coupons
(Note that all specimens were pre-tested in creep and recovery for subsequent
scaling of sample-to-sample stiffness variability)

σ_{max} MPa (ksi)	No. of specimens per R per σ	Fatigue ratio, R	Frequency (Hz)	Maximum no. of cycles
50 (7.25)	3	0, 0.1, 0.3	1	2000
75 (10.9)	3	0, 0.1, 0.3	1	2000
100 (14.5)	3	0, 0.1, 0.3	1	2000
125 (18.1)	3	0, 0.1, 0.3	1	2000

As noted in the foregoing sections, all coupons were subjected to creep and recovery tests at $\sigma = 25$ *MPa* prior to cyclic loading in order to evaluate the scatter in their properties and thereby scale out the sample-to-sample variability.

Results for $R = 0, 0.1$, and 0.3, each at four levels of σ_{max}, are shown in Figs. 27, 28, and 29, respectively. In those figures, the bold faced numbers denote stress levels that correspond to ε_{max}, while the plane numbers are associated with ε_{min}. Note that at $\sigma_{max} = 125$ *MPa* all coupons failed prior to 2000 *cycles*, while at $\sigma_{max} = 100$ *MPa* failure occurred only at $R = 0$. It is also possible to observe the sharp upswings in strains vs. number of cycles upon the approach of failure, as well as the trend towards widening of scatter bands with amplitude of σ_{max}.

As noted previously [1,3], it is possible to relate the strain response to cyclic stress input with growing damage which, for power-law creep, results in the following form.

$$\varepsilon(t) = D_o\eta(t)\sigma(t) + D_1\int_0^t (t-\tau)^n \frac{d}{d\tau}[\eta(\tau)\sigma(\tau)]d\tau \ . \tag{9}$$

Obviously, for cyclic input it is possible to relate time to the number of cycles.

In Eq. (9), damage η was measured as the cycle-to-cycle enhancement in compliance. Thus, for the ith cycle

$$\eta_i = \frac{S_i}{D_o} = \frac{1}{D_o}\frac{\varepsilon_i^{max} - \varepsilon_i^{min}}{\sigma_{max} - \sigma_{min}} \ . \tag{10}$$

Scaling was affected relative to the initial compliance in the linear range, D_o, which was specific to each sample. Values of η_i for $R = 0, 0.1$, and 0.3 at each of the corresponding stress levels are shown in Figs. 30, 31, and 32, respectively, vs. number of cycles i.

It was possible to represent the family of curves shown in the latter figures by an empirical power-law form, namely

$$\eta_i = 1 + (\Delta w_o + \Delta w_1 i^m)H(\sigma - \sigma_d) \ . \tag{11}$$

7

Employment of "best fit" subroutines resulted in sets of values for Δw_o, Δw_1, and m shown in Figs. 33, 34, and 35. In turn, these sets could be related by means of the following empirical expressions:

$$f(\sigma, R) = A + B\sigma + CR + D\sigma^2 + E\sigma R + FR^2 + G\sigma^2 R + H\sigma R^2 + I\sigma^2 R^2 \; , \tag{12}$$

where values of $A, B, ..., I$ for Δw_o, Δw_1, and m are listed in Table 5. These values correspond to σ in *MPa*.

Although damage growth occurs throughout the loading history, its increments were recorded only intermittently, namely over the unloading range of each cycle. In fact, a more detailed experimental evaluation of damage growth may be nearly impossible. For this reason, it is assumed herein that all damage growth, within each individual loading cycle, is focused at the time when $\sigma = \sigma_{max}$. This assumption appears to be a reasonable approximation, since damage is strongly governed by stress.

Table 5. Polynomial fits for the damage parameters Δw_o, Δw_1, and m in Eq. (12)

Coefficients	Δw_o	Δw_1	m
A	-4.8726E-02	2.6291E-03	1.0682E-01
B	1.6740E-03	1.5632E-04	1.7360E-03
C	1.0254E-06	-2.2792E-06	1.6120E-06
D	1.7061E-09	1.3295E-09	-1.6950E-09
E	1.1319E-06	-5.3333E-08	-2.9198E-7
F	2.8071E-02	1.4010E-02	-8.1695E-02
G	4.3893E-07	-1.7871E-06	-5.3496E-06
H	-5.6754E-03	-2.8800E-05	2.2227E-03
I	-3.4439E-06	4.2741E-07	-4.0188E-05

The above assumption implies that damage growth is introduced incrementally, via $\Delta\eta_i$, where

$$\Delta\eta_i = \eta_i - \eta_{i-1} = \Delta w_1 [i^m - (i-1)^m] \qquad i \geq 1 \; . \tag{13}$$

Consequently

$$\eta_N = \eta(t_N) = \Delta w_o H(t) + \sum_{i=1}^{N} \Delta\eta_i H[t - (k + 2i - 1)a] \; . \tag{14}$$

Note, that insertion of Eq. (14) into the convolution integral (9) results in substantial computational simplifications, since integrations now incorporate step and Dirac delta functions.

Consider now the "saw-tooth" stress history shown in Fig. 26(a). For computational purposes it is advantageous to introduce $\hat{t} = t - t_o$, $\hat{\sigma} = \sigma - \sigma_L$, whereby the stress rate is $r = \dfrac{\sigma_L}{t_o} = \dfrac{\sigma_u - \sigma_L}{a} = \dfrac{\hat{\sigma}_u}{a}$, where $t_o = ka$.

The stress-time variation can be expressed by

$$\hat{\sigma}(\hat{t}) = \begin{cases} r(\hat{t} - 2ia) & ia < \hat{t} < (2i+1)a \\ -r[\hat{t} - 2(i+1)a] & (2i+1)a < \hat{t} < 2(i+1)a \end{cases} \quad i = 0, 1, ... \tag{15}$$

resulting in

$$\sigma(t) = rt[H(t) - H(t - t_o)] + rt_o H(\hat{t}) + \hat{\sigma}(\hat{t})H(\hat{t}) \; . \tag{16}$$

Upon a straightforward manipulation one obtains

$$\frac{d\sigma}{dt} = r[H(t) - H(t - t_o)] + \frac{d\hat{\sigma}(\hat{t})}{d\hat{t}} H(\hat{t}) \tag{17}$$

thereby

$$\frac{d\sigma}{dt} = r[H(t) - H(t - t_o)] + \begin{cases} r & ia < \hat{t} < (2i+1)a \\ -r & (2i+1)a < \hat{t} < 2(i+1)a. \end{cases} \quad i = 0,1,\ldots \tag{18}$$

Upon utilization of Eqs. (9)-(18), with expression (14) re-cast in terms of $\hat{t}$, and performing several tedious integrations one obtains

$$\varepsilon_j^{\min} = \varepsilon[t = ka + 2(j+1)a] = \varepsilon[\hat{t} = 2(j+1)a] = I_1 + I_2 + I_3 + I_4 + I_5; \quad j = 0,1,\ldots \tag{19}$$

where

$$I_1 = D_o \sigma_L \eta_{j+1}$$

$$I_2 = \frac{D_1 r}{n+1}\left\{[2(j+1)a + ka]^{n=1} - [2(j+1)a]^{n+1}\right\}$$

$$I_3 = D_1 \sum_{i=0}^{j} \frac{r}{n+1}\left\{-[2(j+1)a - (2i+1)a]^{n+1} + [2(j+1)a - 2ia]^{n+1}\right\}\eta_{i+1}$$

$$I_4 = D_1 \sum_{i=0}^{j} \frac{r}{n+1}\left\{[2(j+1)a - 2(i+1)a]^{n+1} - [2(j+1)a - (2i+1)a]^{n+1}\right\}\eta_{i+1}$$

$$I_5 = D_1[2(j+1)a]^n \sigma_L \eta_o + D_1 \sigma_L \sum_{i=0}^{j} \left\{[2(j+1)a - (2i+1)a]^n\right\}(\eta_{i+1} - \eta_i)$$

and

$$\varepsilon_j^{\max} = \varepsilon[t = ka + (2j+1)a] = \varepsilon[\hat{t} = (2j+1)a] = J_1 + J_2 + J_3 + J_4 + J_5; j = 1,2,\ldots \tag{20}$$

where

$$J_1 = D_o \sigma_u \eta_j$$

$$J_2 = \frac{D_1 r}{n+1}\left\{[ka + (2j+1)a]^{n=1} - [(2j+1)a]^{n+1}\right\}$$

$$J_3 = D_1 \sum_{i=0}^{j} \frac{r}{n+1}\left\{-[(2j+1)a - (2i+1)a]^{n+1} + [(2j+1)a - 2ia]^{n+1}\right\}\eta_i$$

$$J_4 = D_1 \sum_{i=1}^{j} \frac{r}{n+1}\left\{-[(2j+1)a - 2ia]^{n+1} - [(2j+1)a - (2i-1)a]^{n+1}\right\}\eta_i$$

$$J_5 = D_1[(2j+1)a]^n \sigma_L \eta_o + D_1 \sigma_L \sum_{i=1}^{j} \left\{[(2j+1)a - (2i+1)a]^n\right\}(\eta_i - \eta_{i-1}) \quad.$$

Note, however, that in view of Eq. (3), it is necessary to add the permanent component ε_p to $\varepsilon_{\min}$. In view of the cyclic nature of the stress, the value of ε_p was related to the cyclically increasing value of $\varepsilon_{\max}$ according to the expression given in Fig. 6.

The predicted results for $\varepsilon_{\max}$ and $\varepsilon_{\min}$ vs. number of cycles i are shown by the solid lines in Figs. 36, 37, and 38. Note the excellent agreement with the scaled deformation curves. It should be noted that

predictions do depart from data in those cases where failures occurred prior to 2000 load cycles. The above discrepancy is due to the fact that expression (11) does not contain a failure criterion akin to that discussed in Chapter 3.

6. DISTILLED WATER: SORPTION AND EFFECT ON MECHANICAL RESPONSE

This section presents sorption data for the P4 chopped glass/urethane composite exposed to distilled water at several levels of temperature, and the effects of such exposures on mechanical response. Attention is focused on distilled water, since this fluid was shown to provide the most severe environment for a similar composite[6].

6.1 SORPTION BEHAVIOR

The experimental plan involved coupons of the same dimensions as noted previously. All coupons were dried in a desiccating chamber until attaining a stable weight. Subsequently, they were immersed in distilled water at various temperatures, with periodic weight-gain measurements until—and at times beyond—saturation. Randomly selected coupons were then re-dried in a desiccant chamber and weight losses monitored periodically. The exposure schedule is listed in Table 6, and the results are shown in Figs. 39-45.

Table 6. Schedule of exposure to distilled water

Exposure temperature °C (°F)	No. of specimens	Saturation time (hours)$^{1/2}$	Desorption time (hours)$^{1/2}$	Remarks
23 (73)	12^a	85-90^b	30-35 (in progress)	
36 (97)	6	52	27	Some weight loss due to leaching
50 (122)	6	31	22	Noticeable weight loss due to leaching

^{a}Six of these were pre-tested for creep and recovery prior to immersion.
^{b}Estimate.

Note the relatively narrow scatter in both weight-gain and weight-loss data. Figure 39 corresponds to coupons that were not mechanically tested prior to immersion.

The foregoing results lead to the following observations:

(i) Temperature accelerates the diffusion process

Employment of a well-established methodology[7], the data in Figs. 39-42 yield a correlation between the diffusion coefficient D and temperature T, as listed below:

$D(23 \ ^oC) = 5.230 \times 10^{-7} \ mm^2 / sec$, $D(36 \ ^oC) = 1.171 \times 10^{-6} \ mm^2 / sec$,

$D(50 \ ^oC) = 2.634 \times 10^{-6} \ mm^2 / sec$.

A plot of $LogD$ vs. $1/T$ (T in ^oK) is shown in Fig. 46. These results can be represented by:

$$LogD = 2.1165 - \frac{2486.2}{T} \tag{21}$$

where T is in ^oK.

The above values are between one and two orders of magnitude higher than those which obtain for the familiar epoxy resin composites.

(ii) Losses in material integrity increase with exposure temperature

This phenomenon is noted by comparing the weight-gain data shown in Figs. 39-42. These data demonstrate weight-losses that increase with immersion temperature. Furthermore, note the diminishing levels of maximum weight-gains as the foregoing temperature rises. The magnitude of these weight-losses can be determined by comparing weight-gain records against the weight-loss data exhibited in Figs. 43-45. Accordingly, exposure at 36 ^oC results in a net loss of 0.4%, while at 50 ^oC this amount is about 1.2%. These losses are caused by the leaching out of matter from the composite.

6.2 EFFECTS OF IMMERSION ON MECHANICAL RESPONSE

The effects of immersion in distilled water on mechanical response were recorded experimentally by comparing creep and recovery data of test coupons prior to and after their immersion. All data were collected at room temperature under a step stress as noted in Chapter 2, with $\sigma_o = 25\ MPa$ and load duration of $t_o = 30\ min$. Recovery strains were recorded during an additional 90 minutes. Results are shown in Figs. 47-52 and summarized in Figs. 53, 54, and 55.

Note the increase in creep strains when comparing the dry and immersed data, with increasing disparity due to higher immersion temperatures. Furthermore, it can be observed that prior exposure to distilled water results in permanent residual deformation, where none existed in the absence of such exposure. The amplitude of this permanent deformation tends to increase with immersion temperature. The abovementioned enhancements in both creep strains and permanent deformation are clear indicators of fluid-induced irreversible degradations.

7. CONCLUDING REMARKS

An experimental program was performed regarding the response of random P4 chopped glass/urethane resin composite. The program was guided by a theoretical model derived from basic principles of irreversible thermodynamics and continuum mechanics, which was developed to predict the behavior of the specific class of materials investigated herein.

The experimental data were employed to quantify the material parameters included in the theoretical formulation. These parameters accounted for the effects of stress and temperature on the ensuing deformation. With these parameters at hand it was possible to utilize the model in a predictive mode and assess its usefulness through comparisons with responses to more complex inputs. These comparisons proved to be satisfactory.

The foregoing results demonstrate the applicability of the methodology employed herein to a technically significant class of polymeric materials, namely those where creep is accompanied by the formation and growth of a multitude of internal microcracks.

7.1 PRACTICAL IMPLICATIONS

The model presented herein can be utilized in three major ways:

(i) Predict long-term behavior on the basis of short-term data.
(ii) Interpret and employ accelerated deformation data, obtained at elevated temperatures, to assess long-term response.
(iii) Analyze stress-strain response under exposure to fluctuating stress and temperature inputs.

REFERENCES

1. Smith, L. and Weitsman, Y. (1998). "Inelastic Behavior of Randomly Reinforced Polymeric Composites Under Cyclic Loading," *Mechanics of Time-Dependent Materials*, Vol. 1, pp. 293-305.

2. Smith, L. and Weitsman, Y. (1998). "The Visco-Damage Mechanical Response of Swirl-Mat Composites," *International Journal of Fracture* (in print).

3. Elahi, M. and Weitsman, Y. (1999). *Some Aspects of the Deformation Response of Swirl-Mat Composites*, ORNL/TM-13521, Engineering Technology Division, Bldg. 9204-1, MS 8051, Box 2009, Oak Ridge National Laboratory, Oak Ridge, TN 37831-8051.

4. Abdel-Tawab, Kh. and Weitsman, Y. (1998). "A Coupled Viscoelasticity/Damage Model with Application to Swirl-Mat Composites," *International Journal of Damage Mechanics*, Vol. 7, No. 4, pp. 351-380.

5. Abdel-Tawab, Kh. and Weitsman, Y. (1998). "A Strain-Based Formulation for the Coupled Viscoelasticity/Damage Behavior," Contract Technical Report No. MAES97-3.0-CM, Department of Mechanical and Aerospace Engineering and Engineering Science, The University of Tennessee, Knoxville, TN 37996-2030.

6. Corum, J. M., Battiste, R. L., Brinkman, C. R., Ren, W., Ruggles, M. B., and Yahr, G. T. (1998) *Durability-Based Design Criteria for an Automotive Structural Composite: Part 1. Design Rules*, ORNL-6930, Engineering Technology Division, Bldg. 9204-1, MS 8051, Box 2009, Oak Ridge National Laboratory, Oak Ridge, TN 37831-8051.

7. Shen, C.-H. and Springer, G. S. (1980). "Moisture Absorption and Desorption of Composite Materials," in *Environmental Effects on Composite Materials* (G. S. Springer-Editor), Technomic Pub. Co., pp. 15-33.
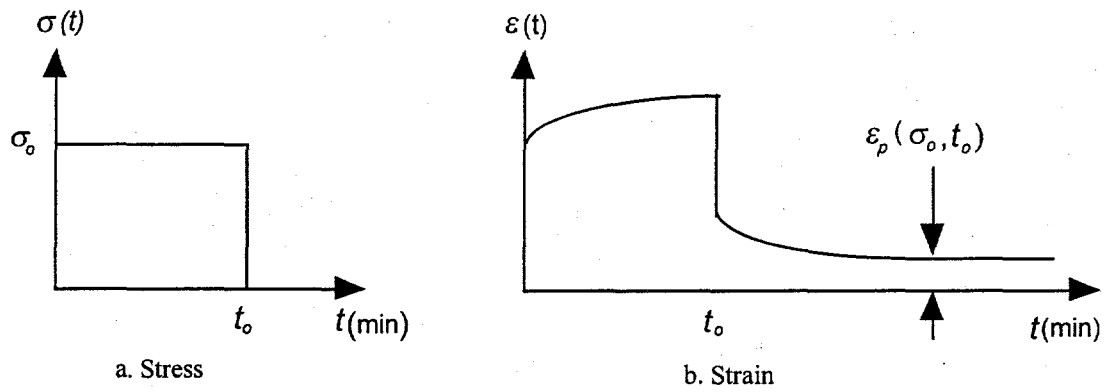
Fig. 1. Schematic drawings of stress input history and strain output.
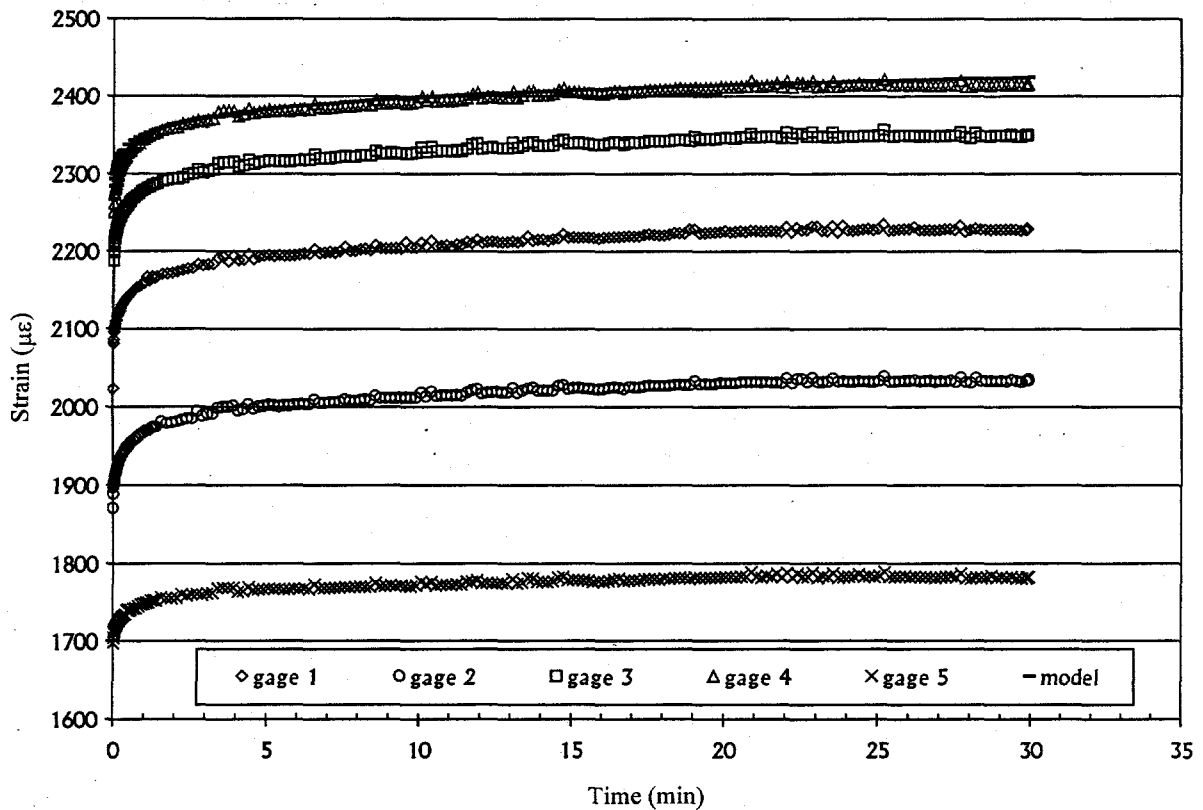
Fig. 2. Creep strains due to σ=25 MPa at five stations along a single coupon, implying a 35% variability in stiffness.
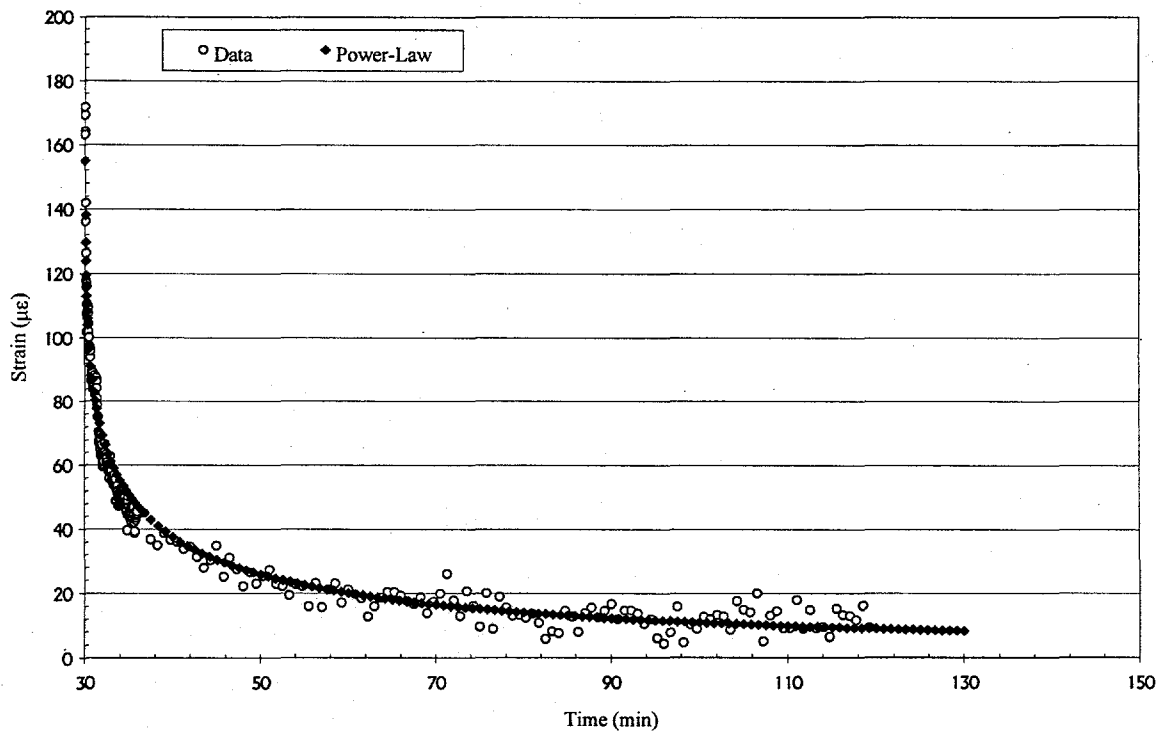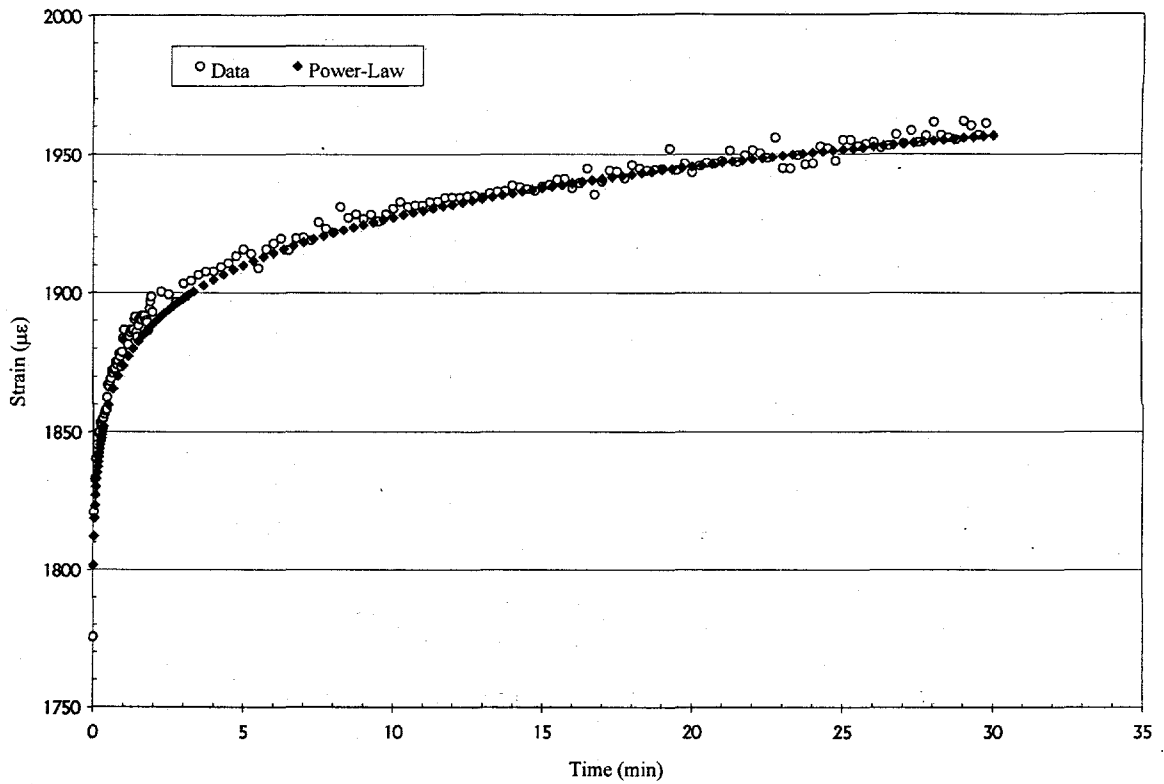
Fig. 3. Typical data for creep (top) and recovery (bottom) within the linear range of response. Data (ooo) and model ($\blacklozenge \blacklozenge \blacklozenge$). σ_0=25 MPa, t_0=30 min., T=23 °C, D_0=6.51x10^{-5} MPa^{-1}, D_1=9.72x10^{-6} MPa^{-1} min^{-n}, and n=0.086.

14
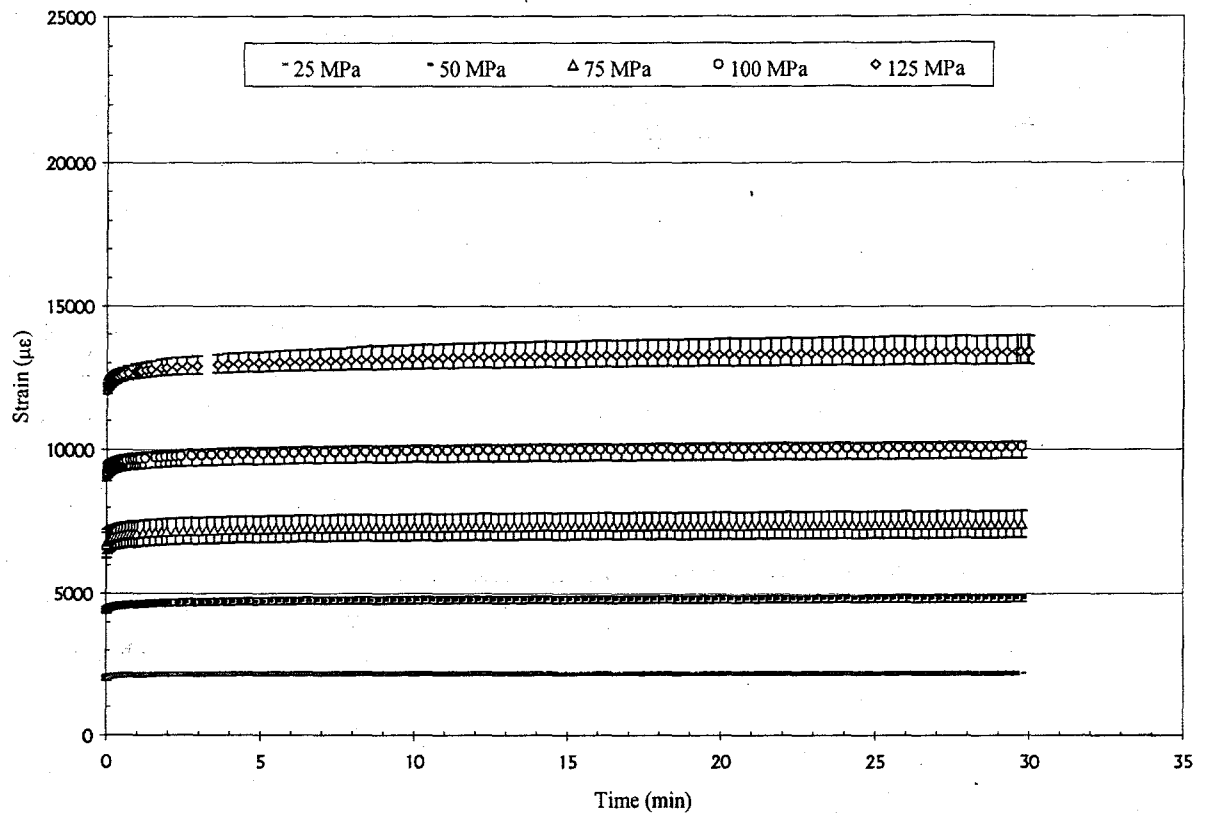
**Fig. 4. Scaled creep data at 23 °C under various stress levels.
Average values and scatter bands.**

15
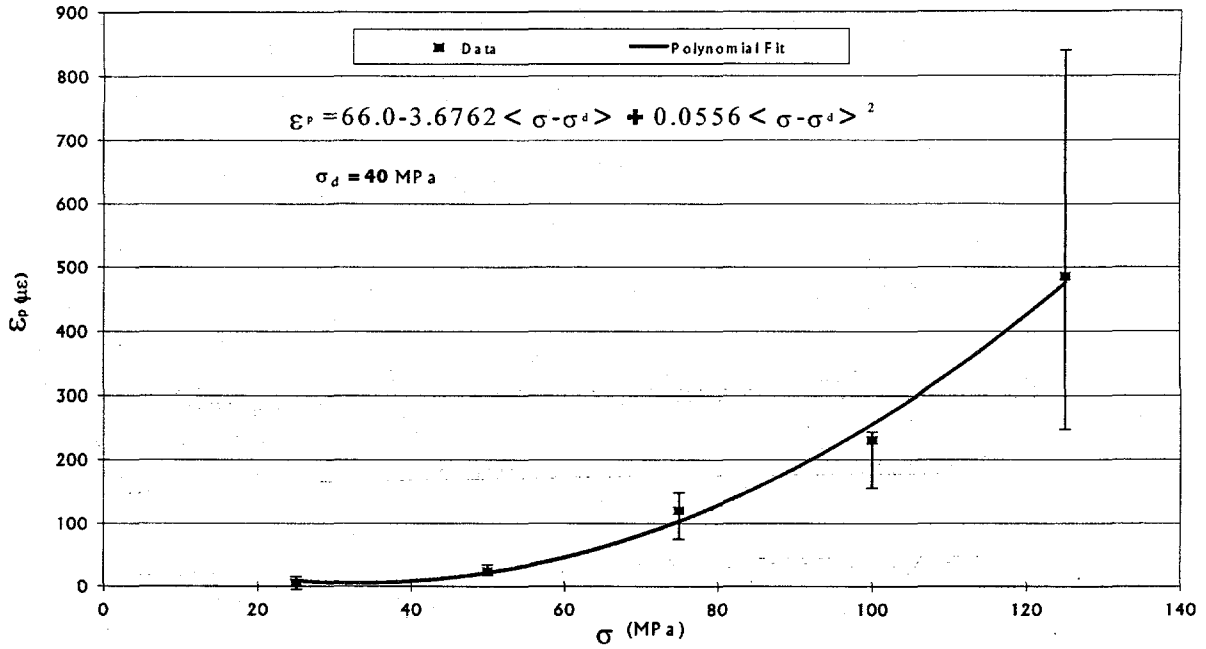
Fig. 5. Permanent residual strain vs. level of applied stress. Average values and scatter bands.
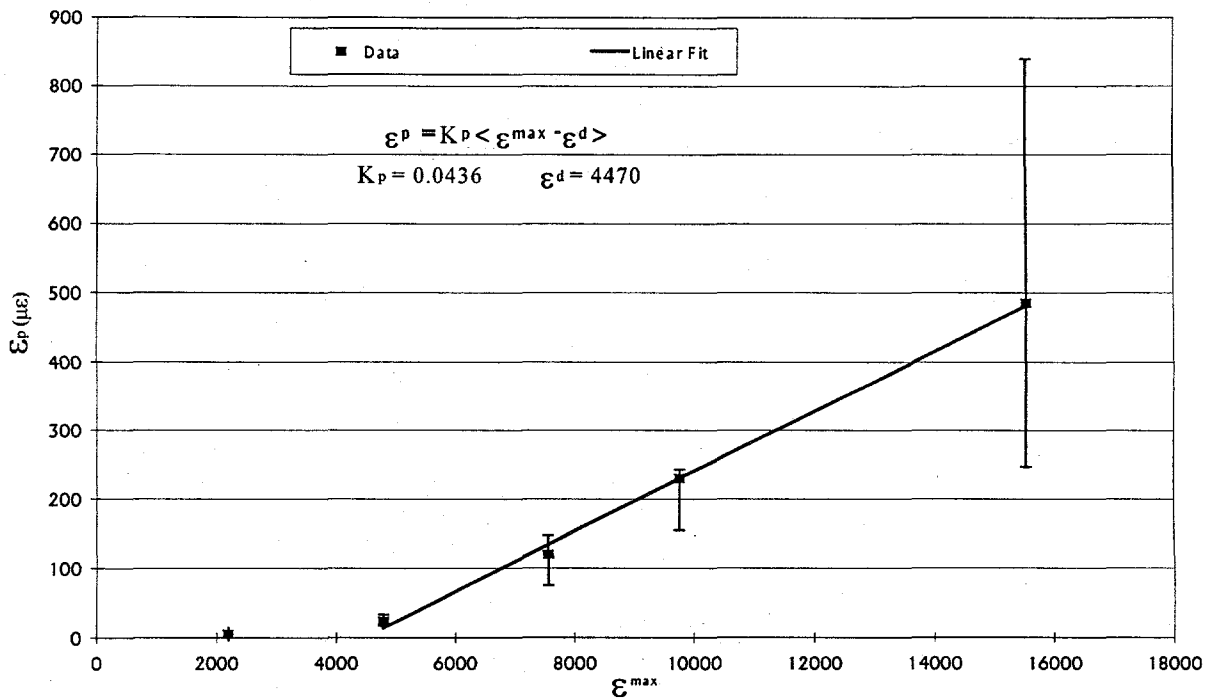
Fig. 6. Permanent residual strain vs. averaged values of maximum strains attained under loading. Average values and scatter bands.

16
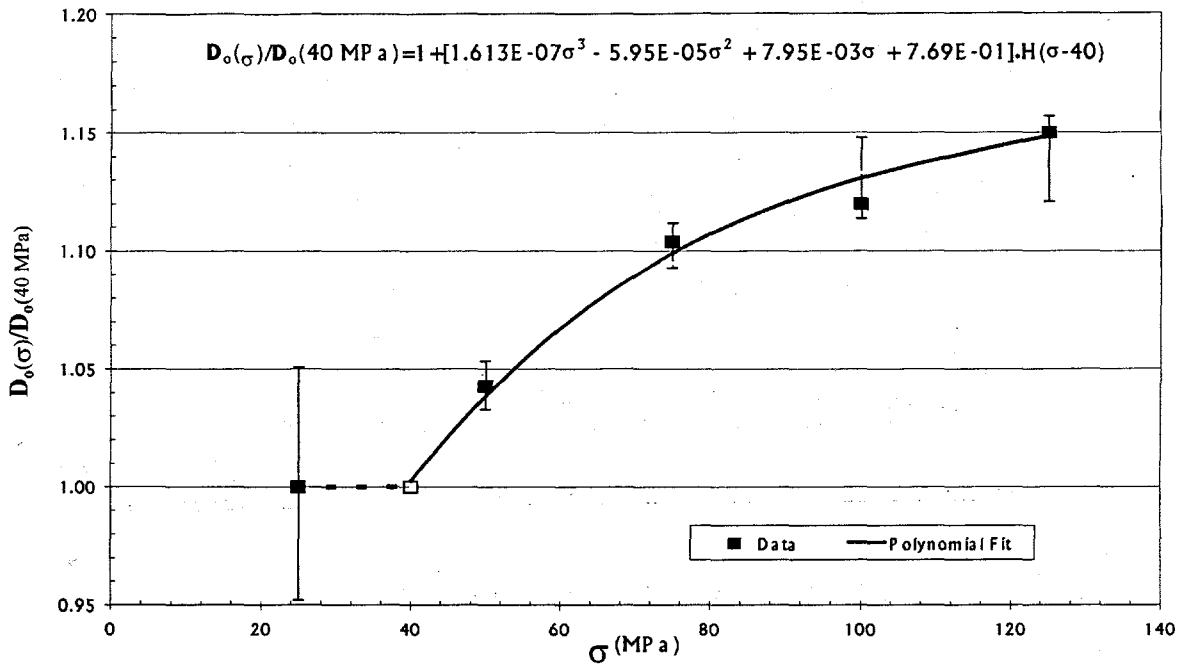
Fig. 7: Scaling factor for $D_o(\sigma)$ to be employed in Eq. (3).
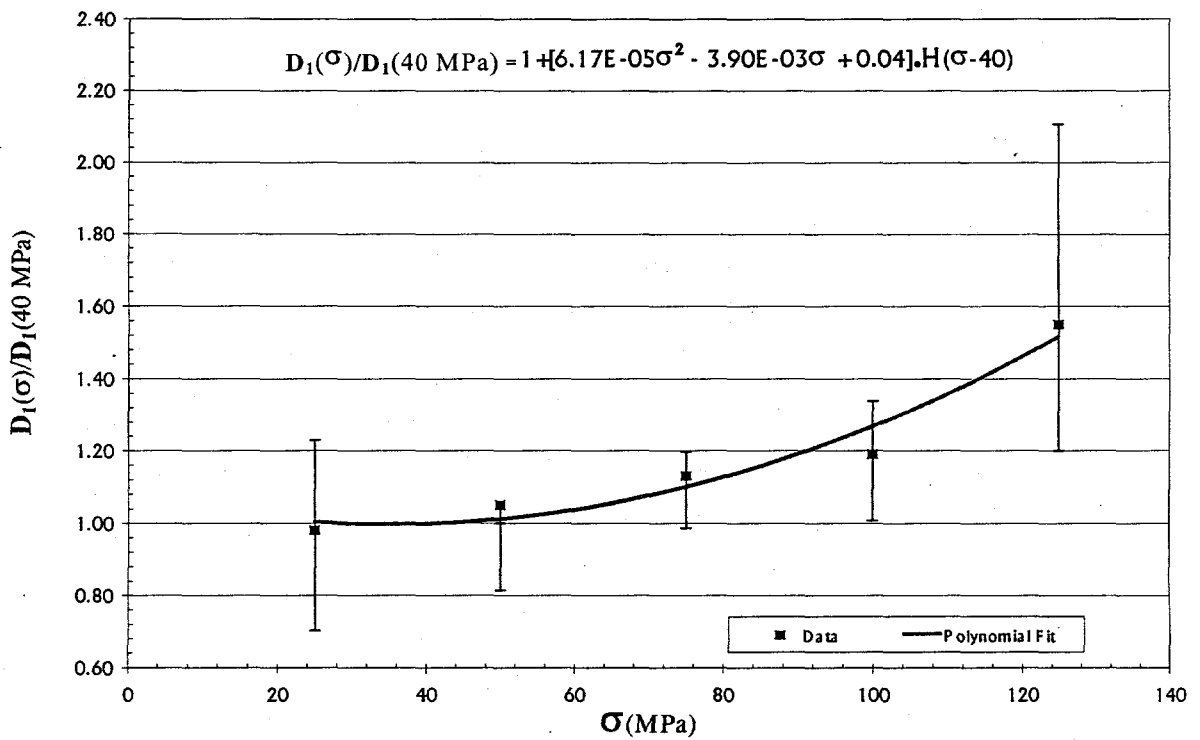
Fig. 8: Scaling factor for $D_1(\sigma)$ to be employed in Eq. (3).

17
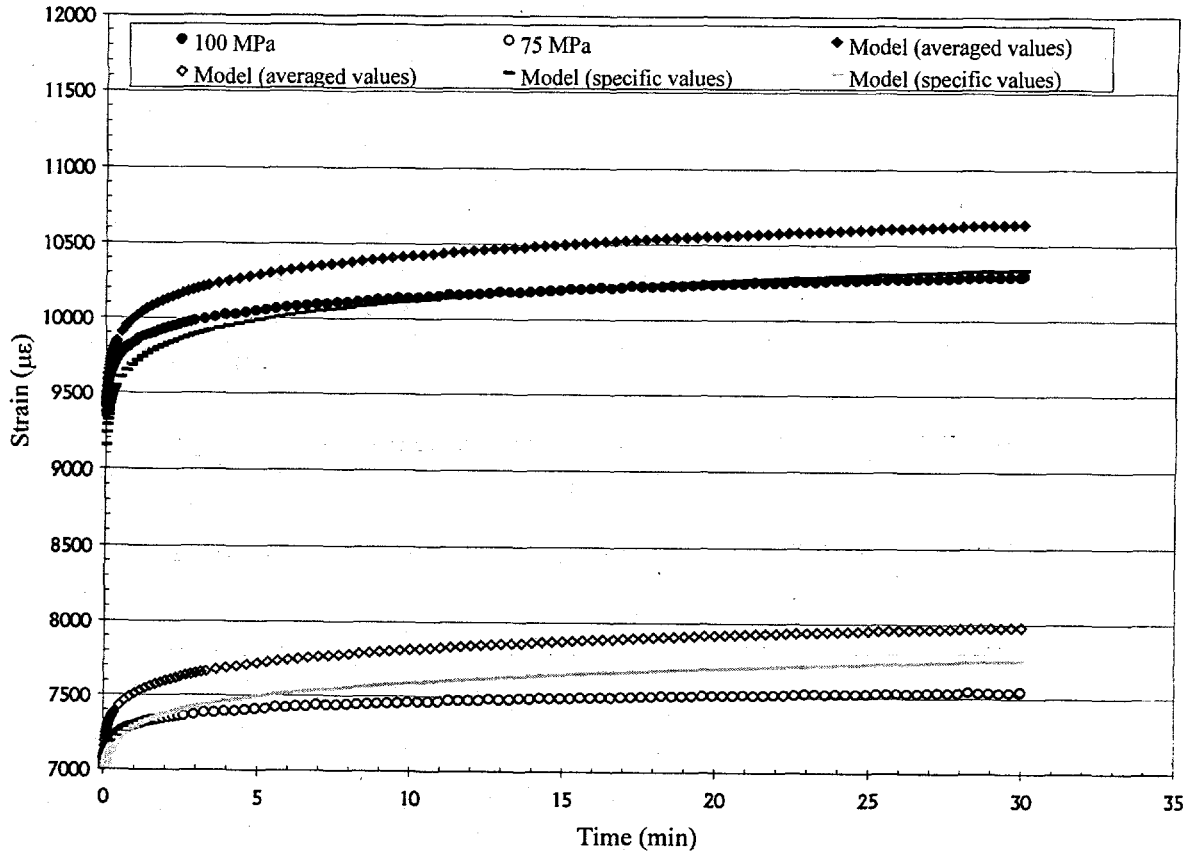
Fig. 9: Two-step stress history model verification test. A step stress σ_1=100 MPa was applied and removed after 30 minutes. Following a relaxation period of 24 hours a second step stress σ_2=75 MPa was applied. Data (○ ●) and model predictions: (i) based upon Eq. (3) (◊ ♦), (ii) based upon best power-law fit for σ_1=100 MPa (---). (Filled symbols σ_1=100 MPa, open symbols σ_2=75 MPa).
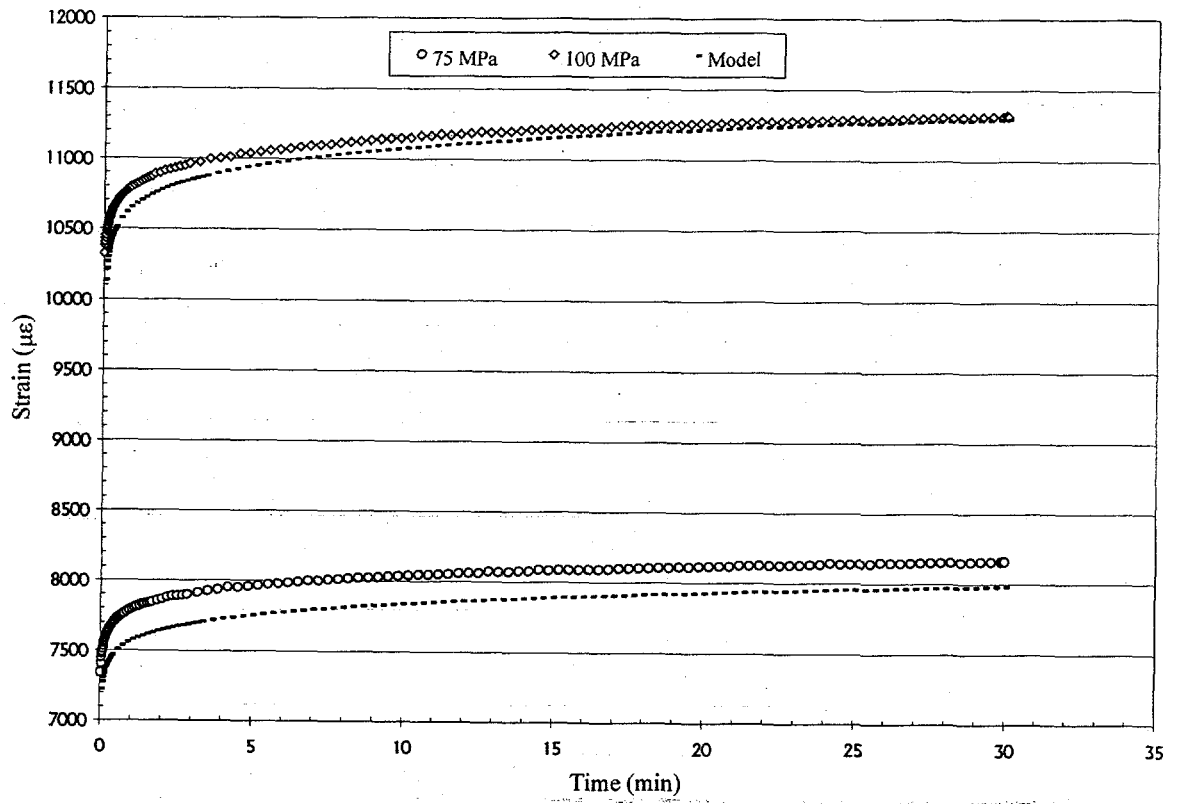
Fig. 10. Same as Fig. (9), but σ_1=75 MPa and σ_2=100 MPa.
Data and predictions are based upon Eq. (3).
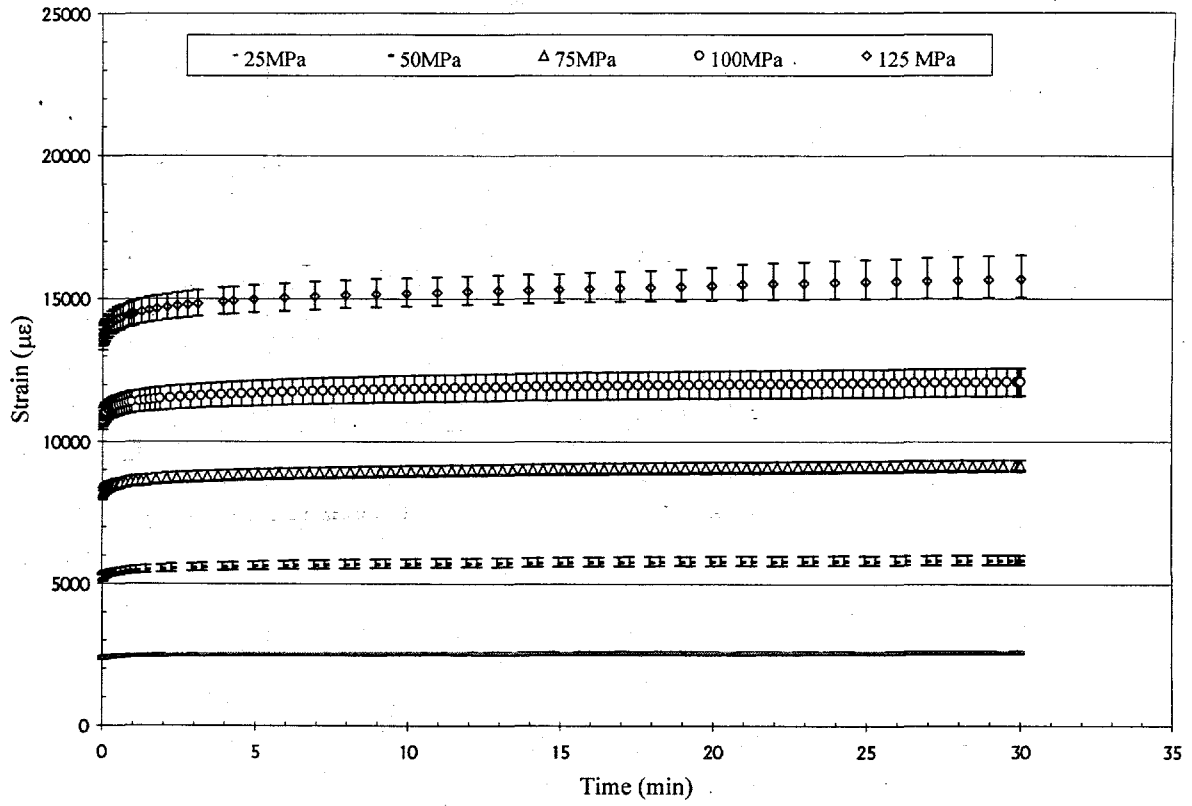
Fig. 11. Scaled creep data at T=50 °C under various stress levels. Average values and scatter bands.
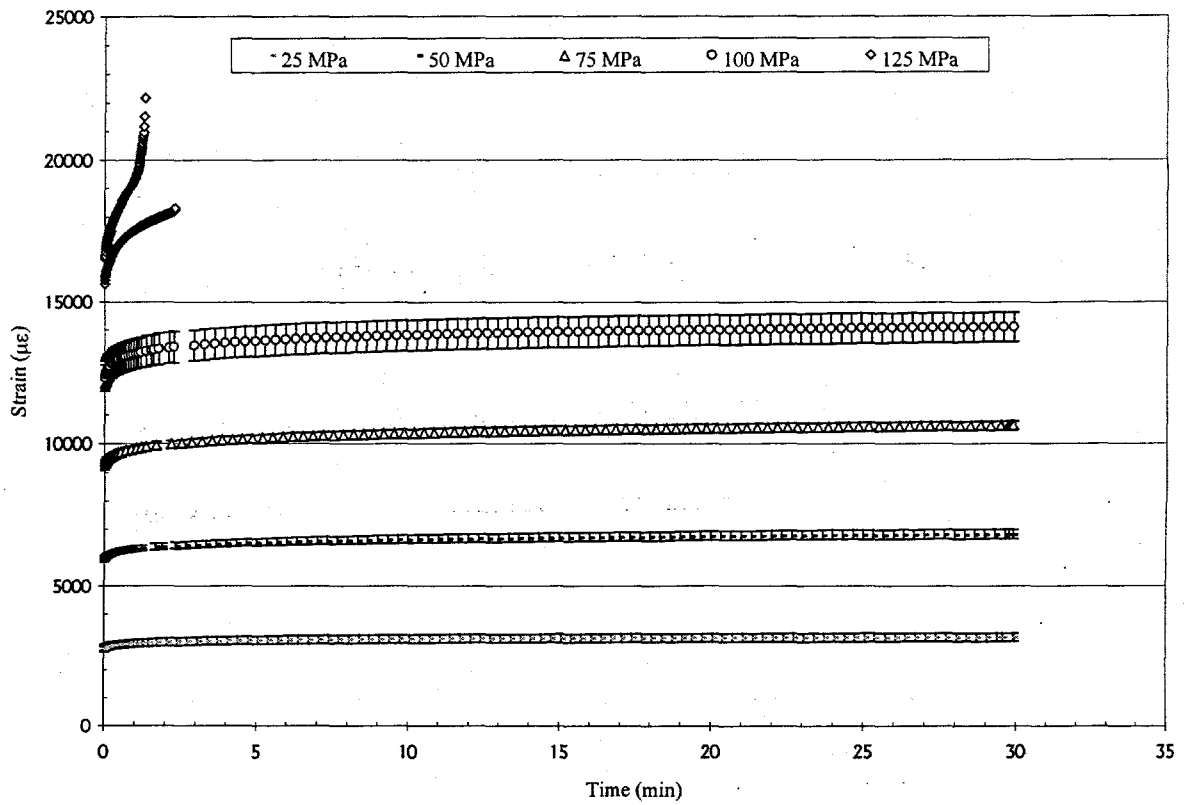
Fig. 12. Scaled creep data at T=120 °C under various stress levels. Average values and scatter bands.

$D_o(T)/D_o(23\ ^oC) = 0.863 + 6.50E\text{-}03T - 2.31E\text{-}05T^2$

$23\ ^oC \leq T \leq 120\ ^oC$
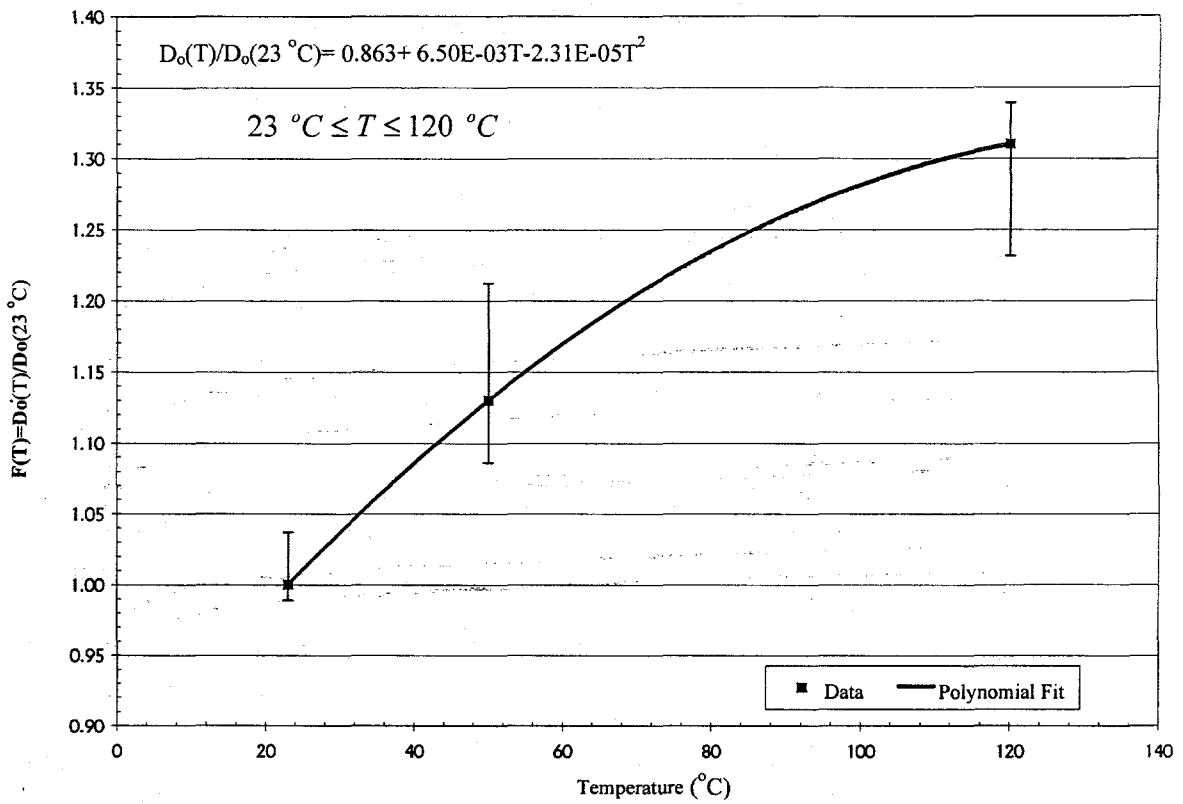
Fig. 13. Temperature-induced enhancement of Do.

$\text{Log}\ a_T = 2.0802 - 9.97E\text{-}02T + 4.01E\text{-}04T^2$

$23\ ^oC \leq T \leq 120\ ^oC$
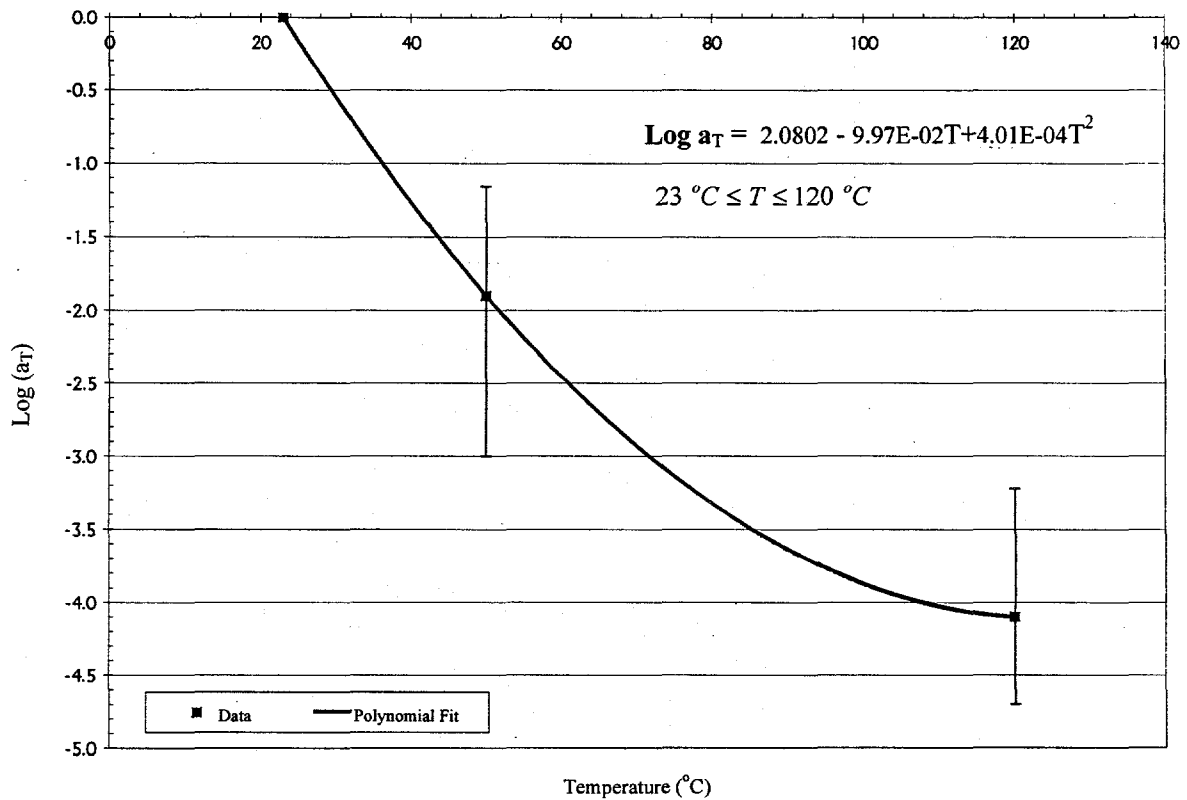
Fig. 14. Time-temperature shift factor aT vs. temperature T.
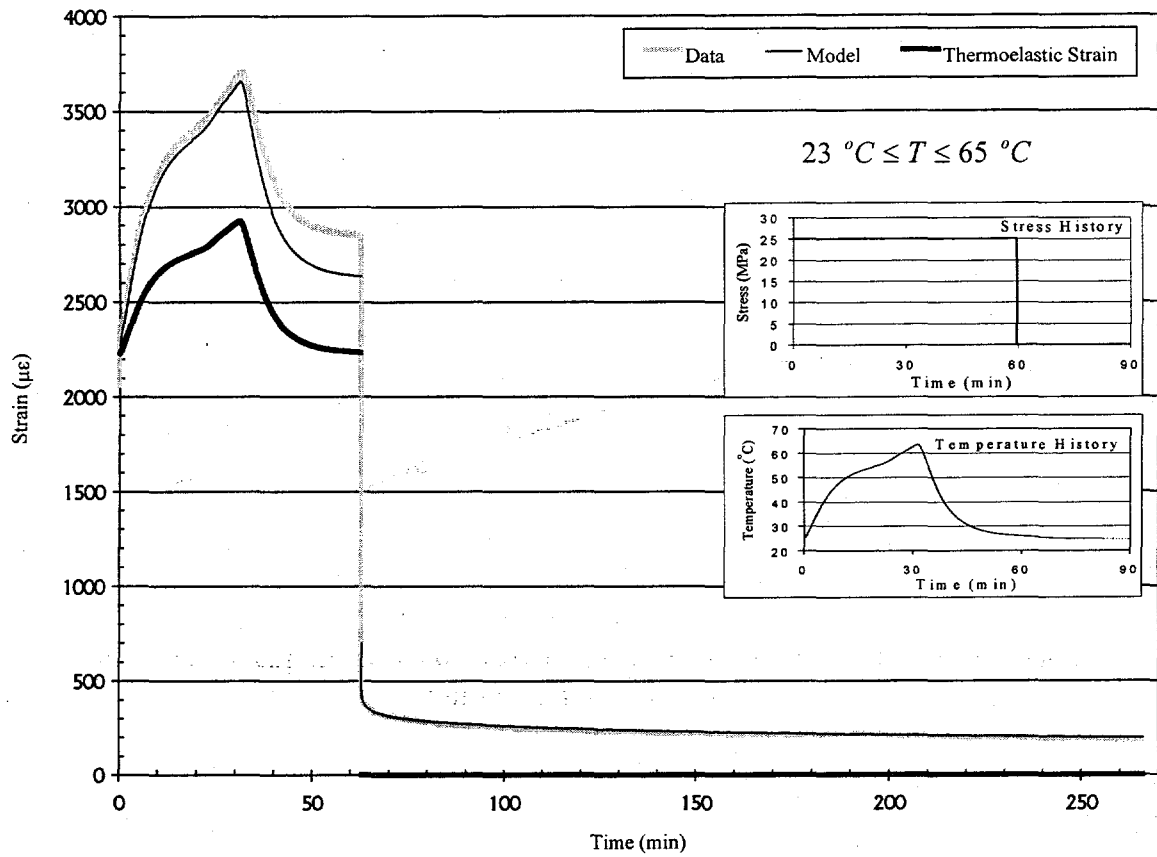
Fig. 15. Varying temperature verification test. Data (▓▓▓▓), model predictions (Eq.(5a)) (——), and thermoelastic predictions (▬▬).
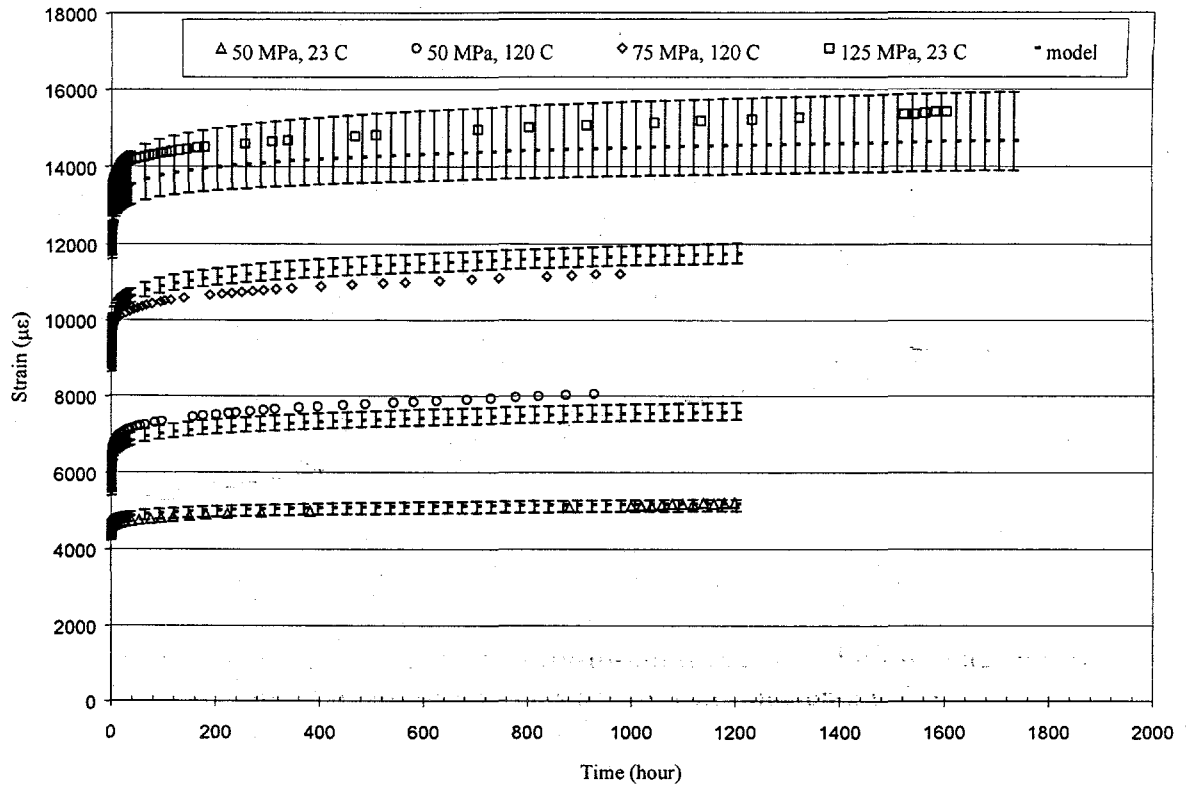
Fig. 16. Long-term creep data (open symbols) at various levels of stress and temperature and predictions based on Eq. (5). Model average values (---) and scatter bands.
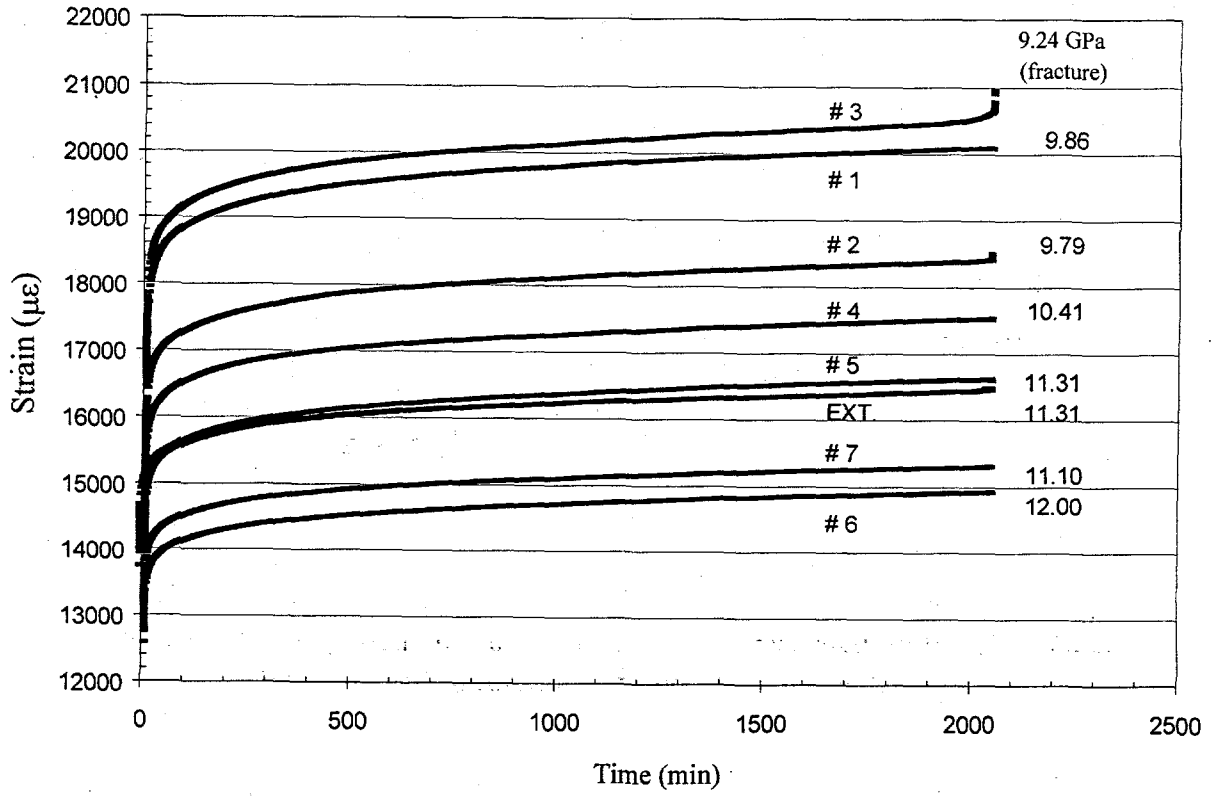
Fig. 17. Creep-to-failure data from a multigaged coupon under a step stress of 130 MPa. Curves numbered no. 1 through no. 7 correspond to positions of strain gages, starting from the top and numbers on the right correspond to stiffness as recorded within the linear range of response. Failure occurred under gage no. 3.
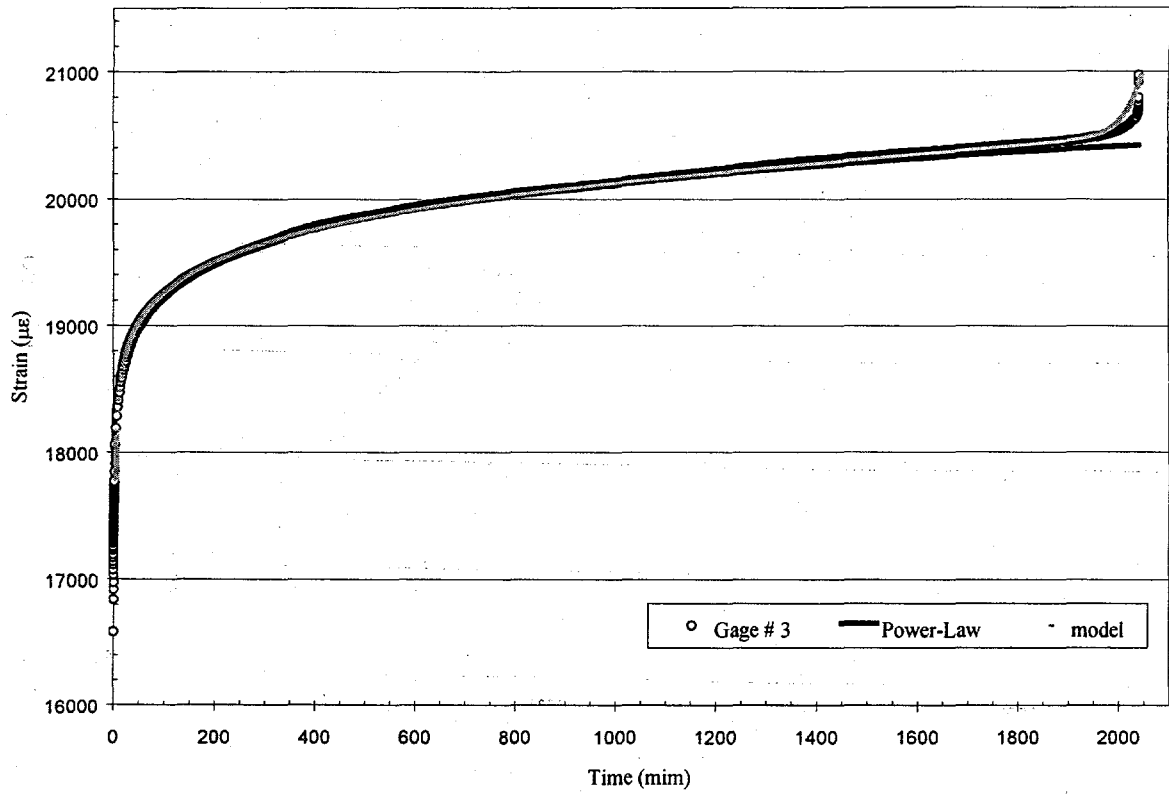
Fig. 18. Creep-to-failure response under gage no. 3 in Fig. 17. Data (ooo), prediction of "best fit" power-law (—), and prediction accounting for damage growth (---).
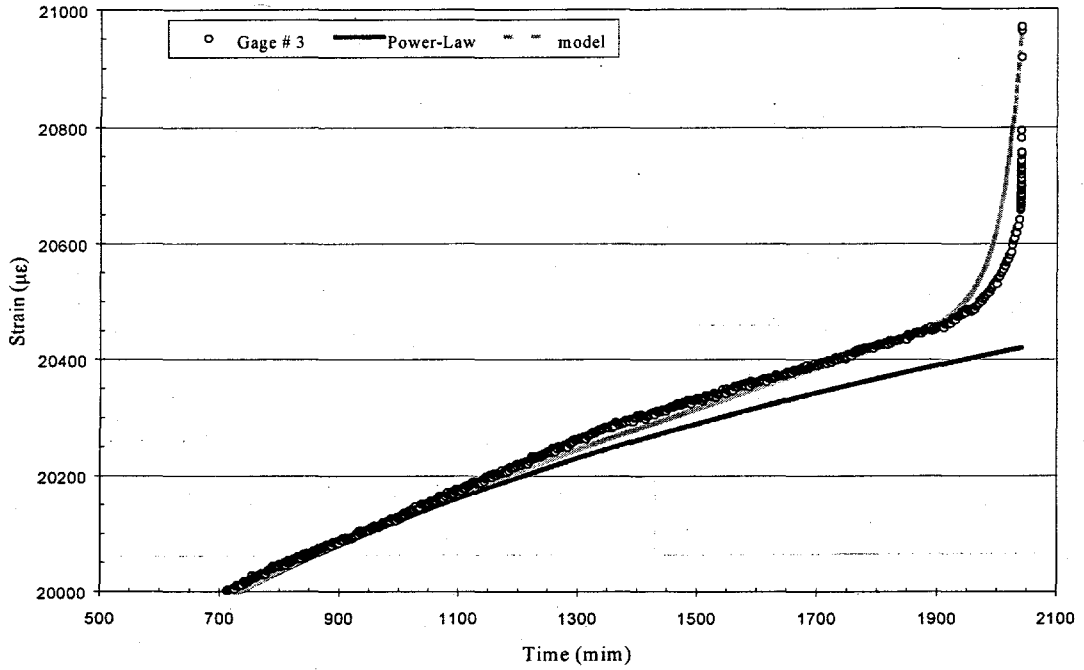
Fig. 19. An expanded view of strain vs. time upon the advent of failure. Symbols same as Fig. 18.
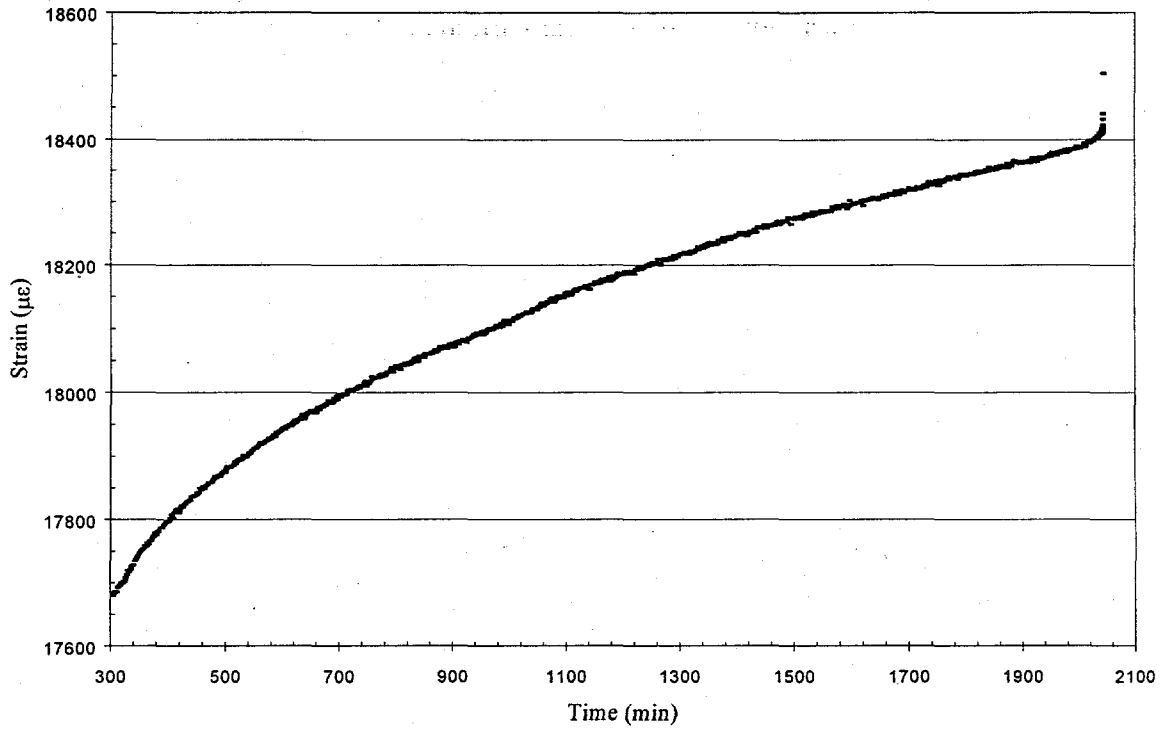
Fig. 20. Strain-to-failure recorded under gage no. 2 in Fig. 17.

27
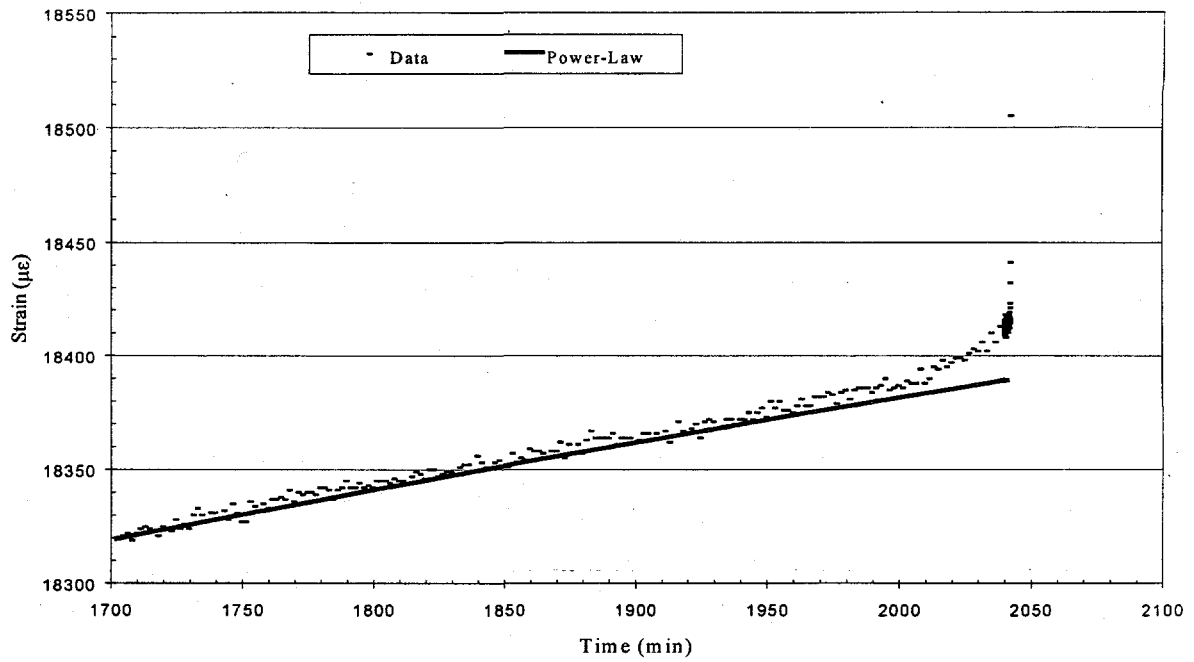
Fig. 21. An expanded view of strain-to-failure recorded under gage no. 2. Data (---) and predictions of "best fit" power-law (—).
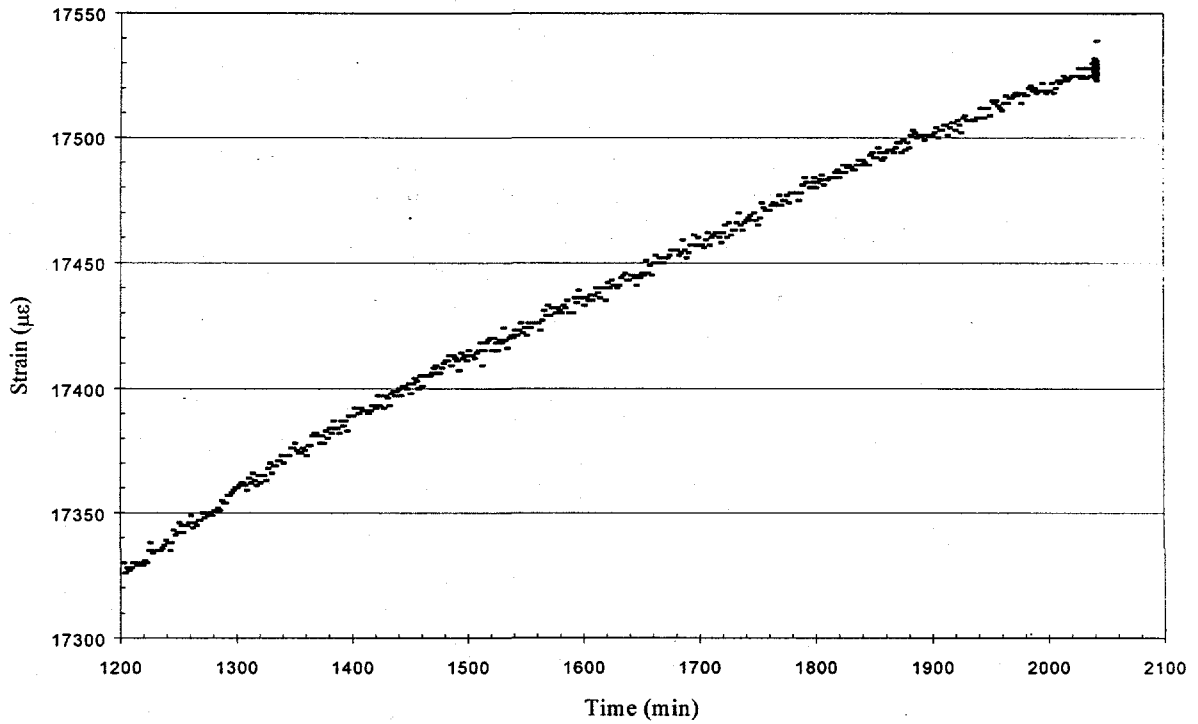
Fig. 22. An expanded view of creep-to-failure data under gage no. 4 in Fig. 17.

28
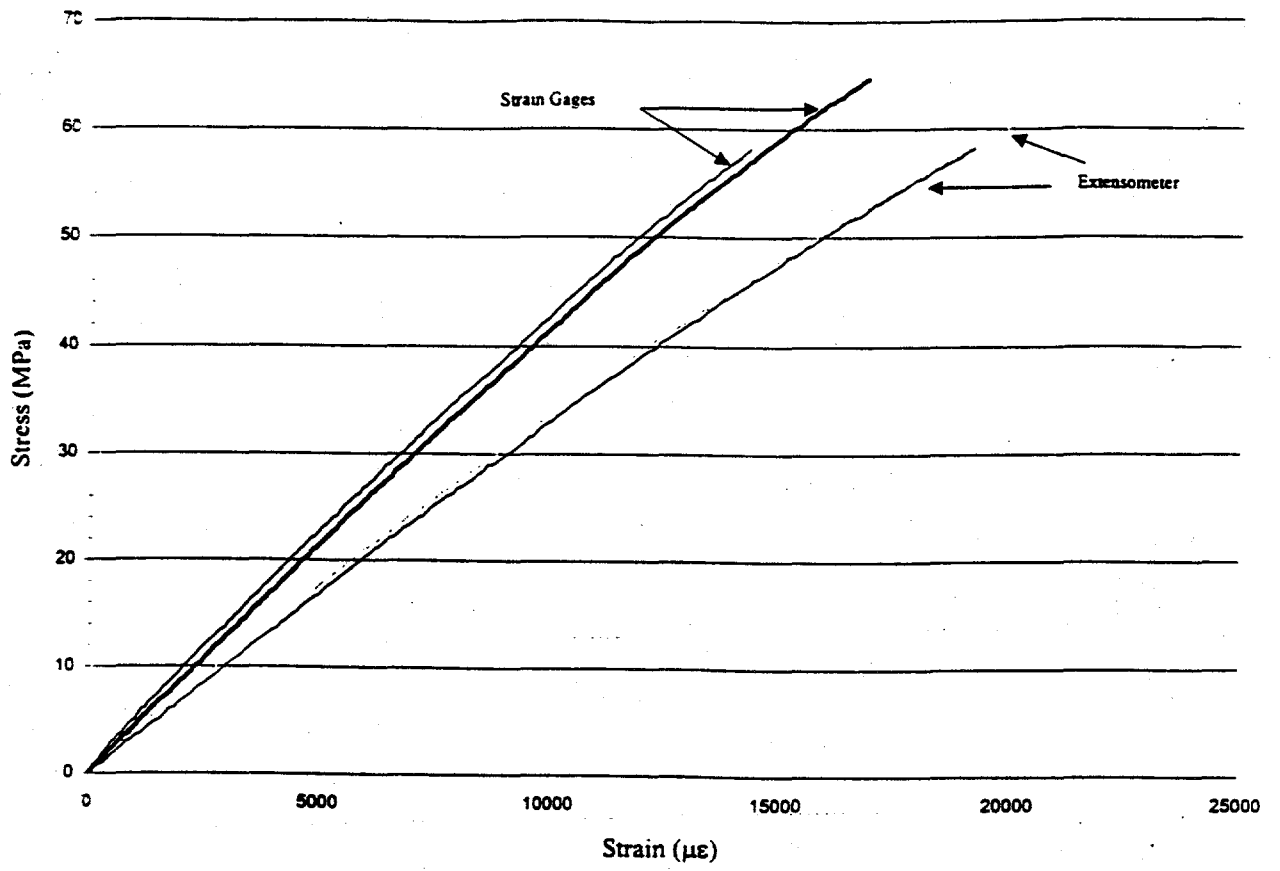
Fig. 23. Stress-strain behavior of urethane (neat resin) specimens.
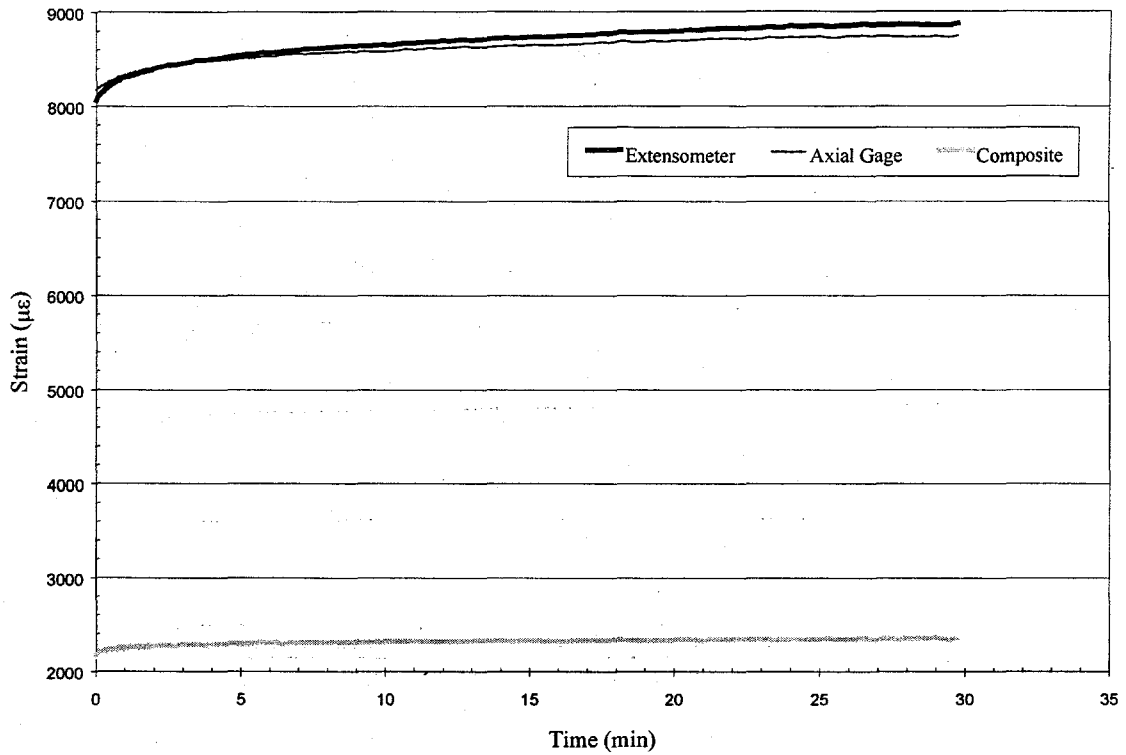
Fig. 24. Creep of urethane neat resin (—) as compared with that of P4 chopped glass/urethane (▬▬) for σ=25 MPa, and T=23 °C. Thick lines exhibit extensometer readings, while the thin line corresponds to strain gage record.
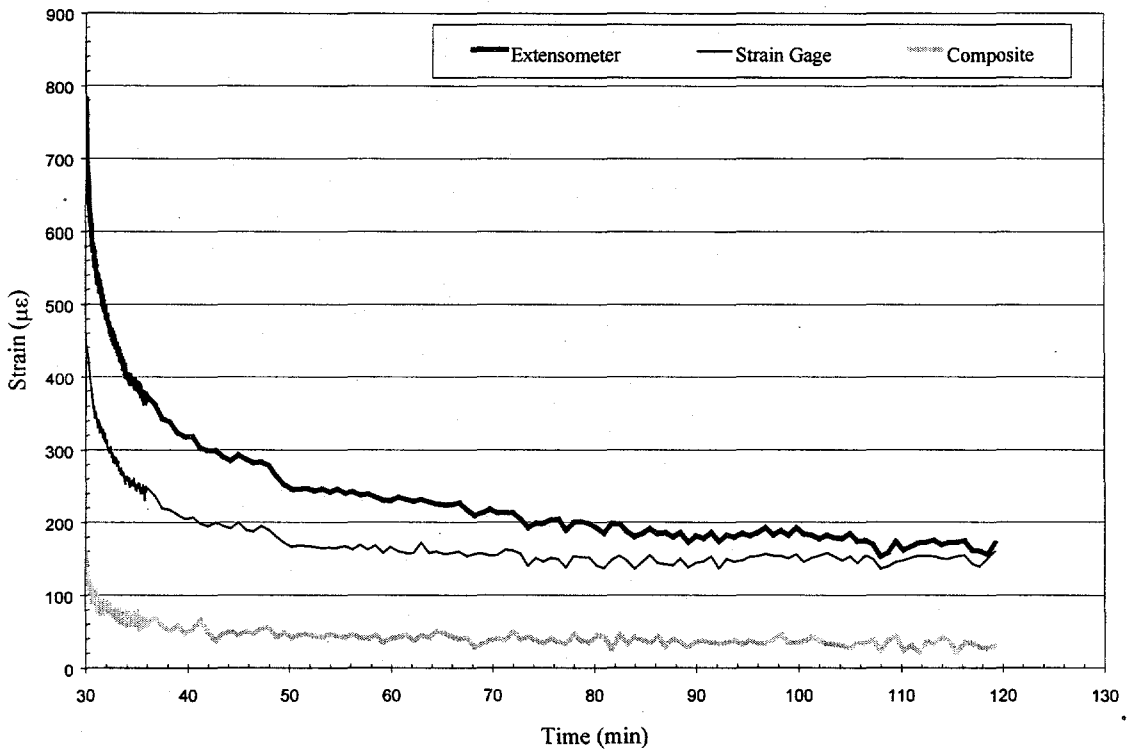
Fig. 25. Recovery data. Symbols same as Fig. 24.

30

a. Saw tooth stress input b. Strain response
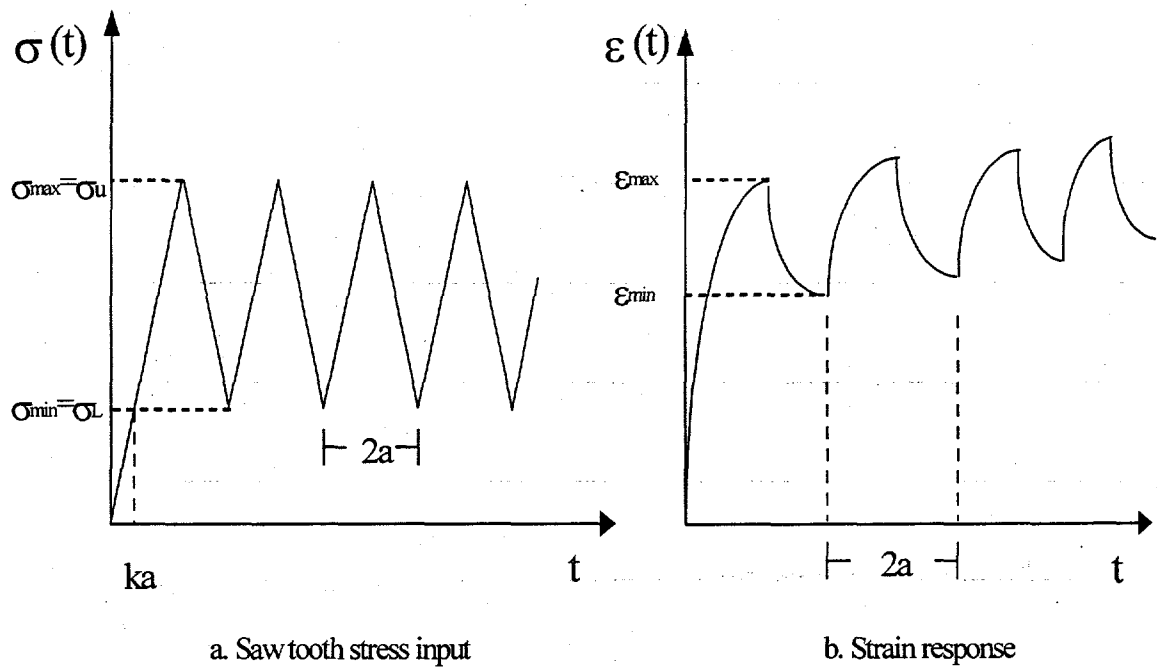
Fig. 26. Schematic diagrams for cyclic testing.
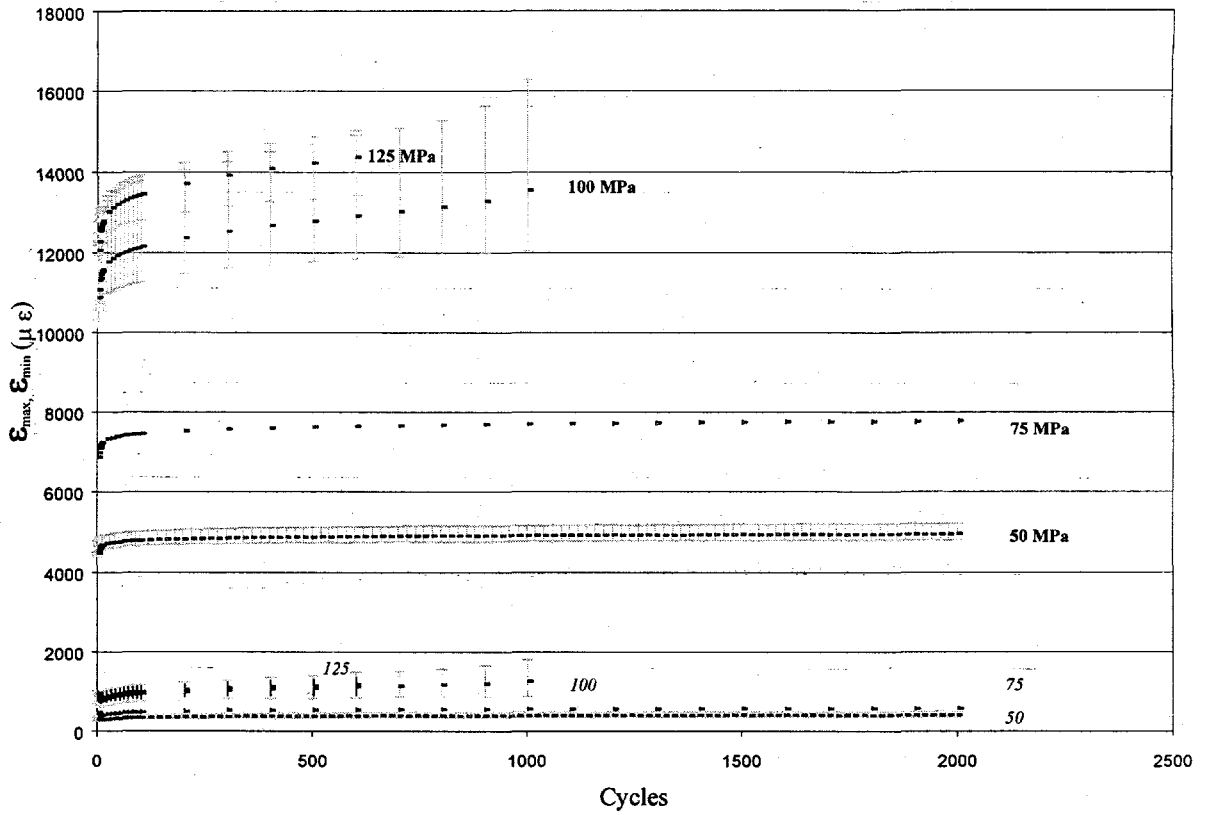
Fig. 27. Unscaled strain data at various levels of maximum stress at R=0, vs. number of cycles. Stress levels shown in bold numbers correspond to maximal strains, and those shown by plain numbers correspond to minimum strains. Average values and scatter bands are shown.
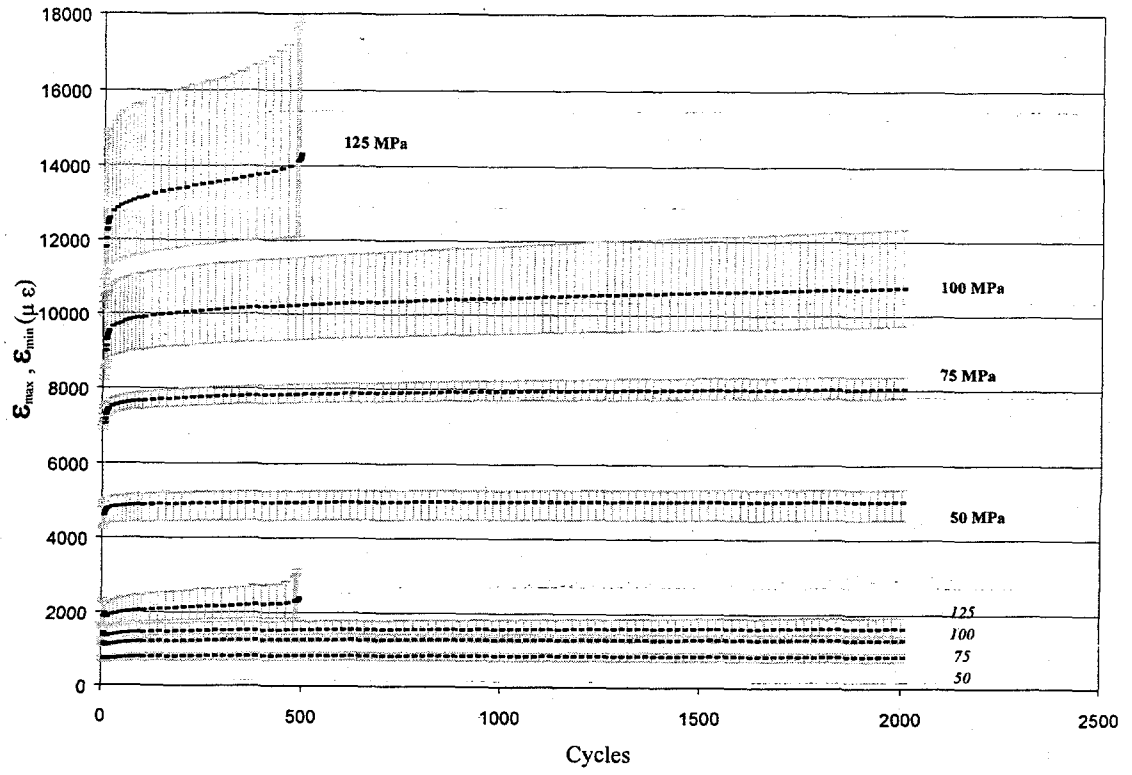
Fig. 28: Same as Fig. 27, but R=0.1.
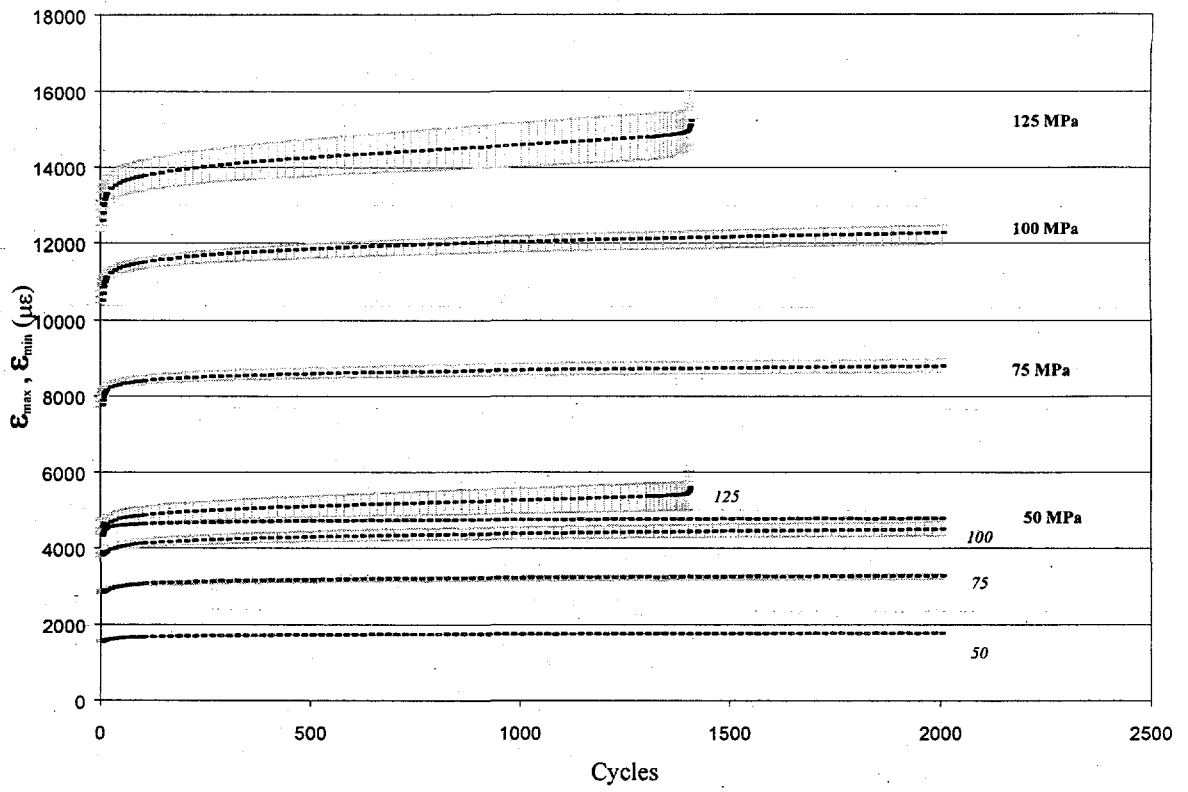
Fig. 29. Same as Fig. 27, but R=0.3.
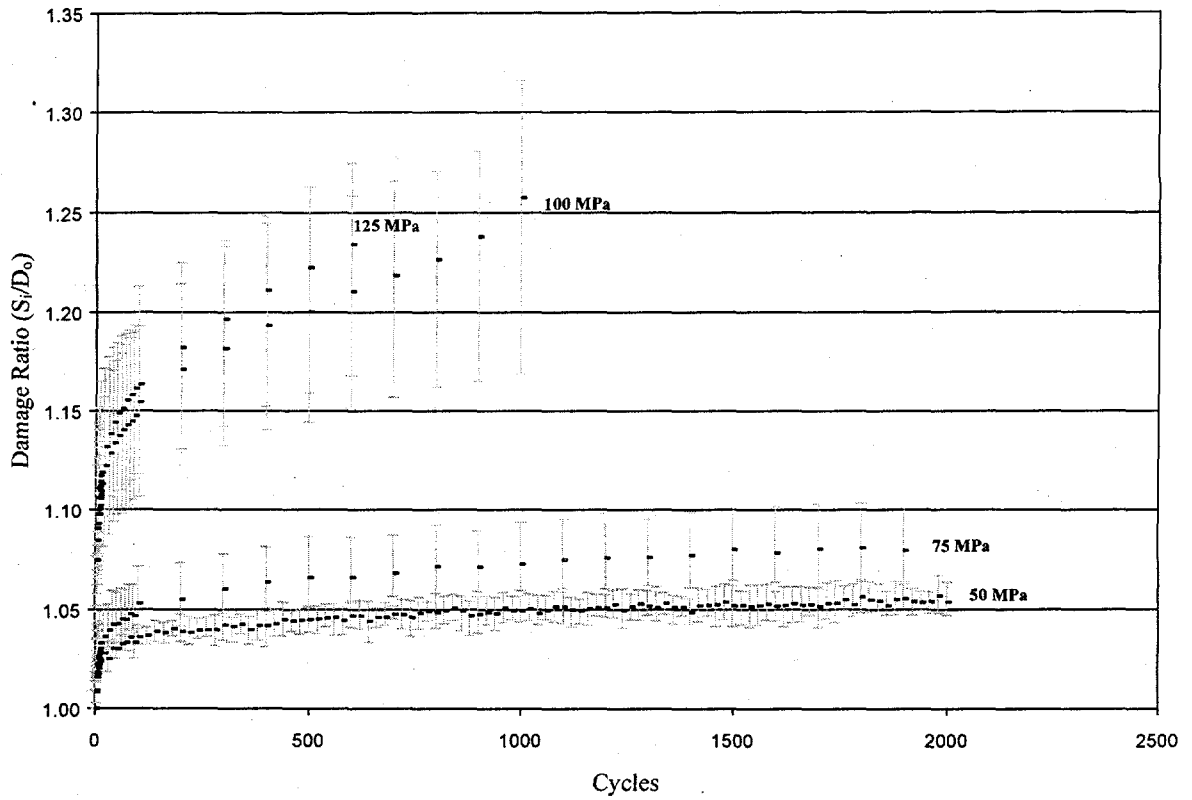
Fig. 30. Ratio of unloading compliance to initial compliance vs. number of cycles for various values of maximal stress with R=0. Average values and scatter bands are shown.
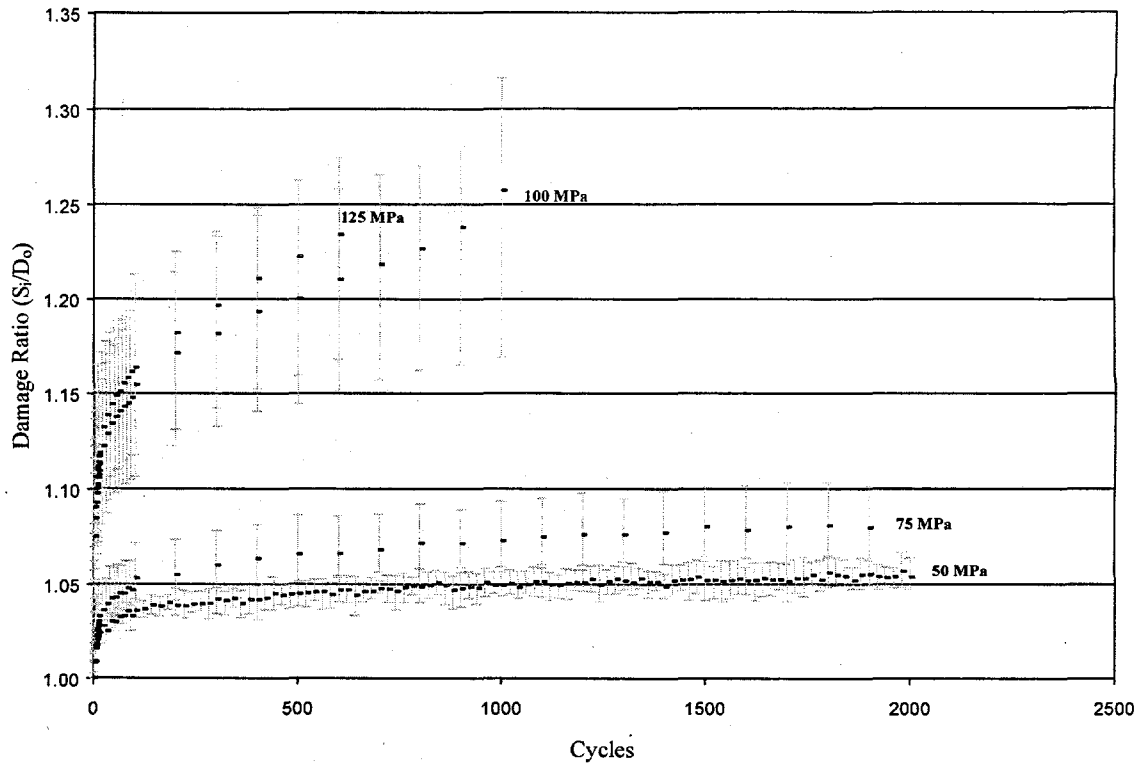
Fig. 31. Same as Fig. 30, but R=0.1.
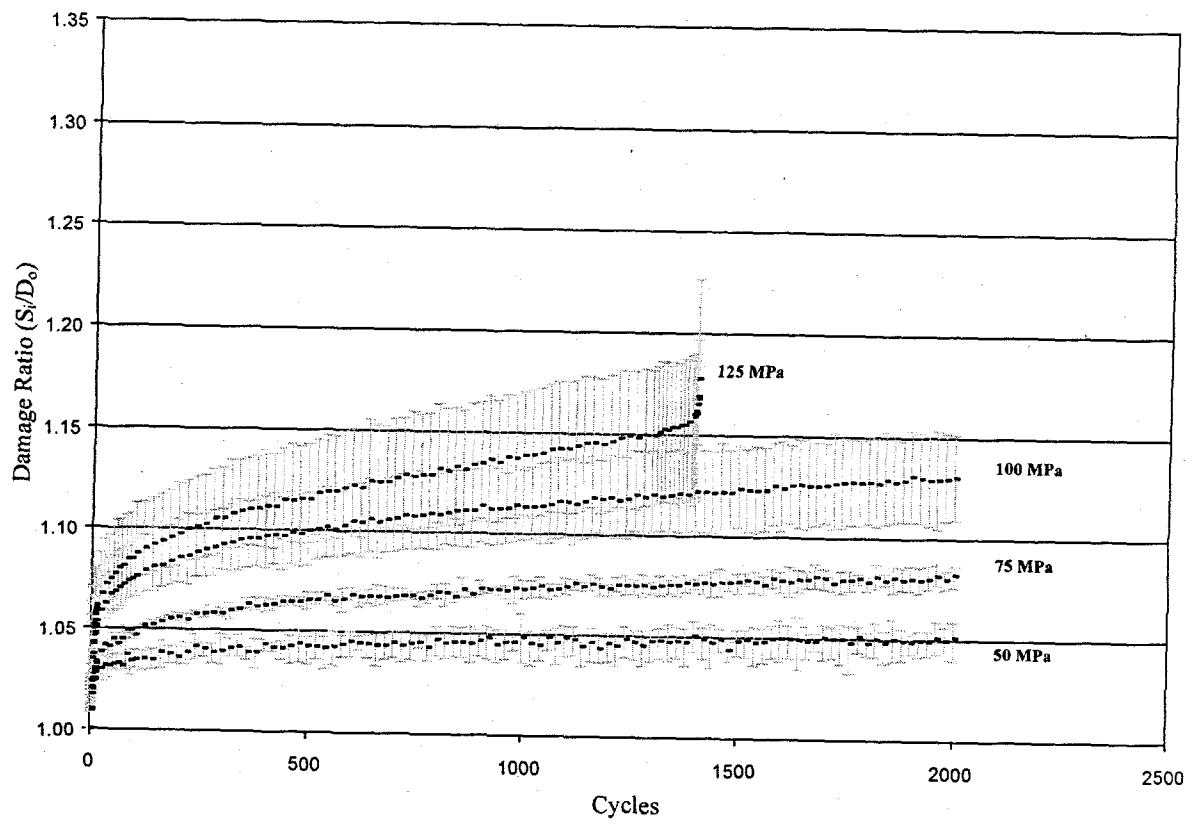
Fig. 32. Same as Fig. 30, but R=0.3.
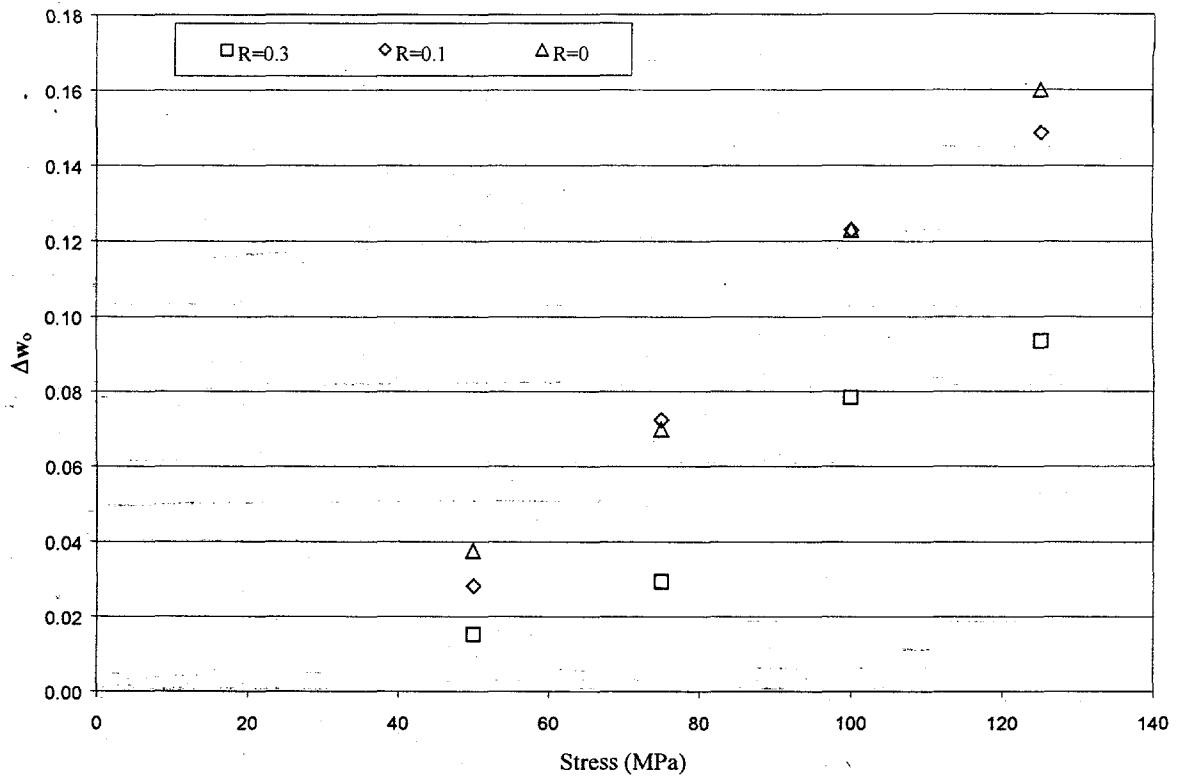
Fig. 33. Damage parameter Δw_o vs. stress σ.
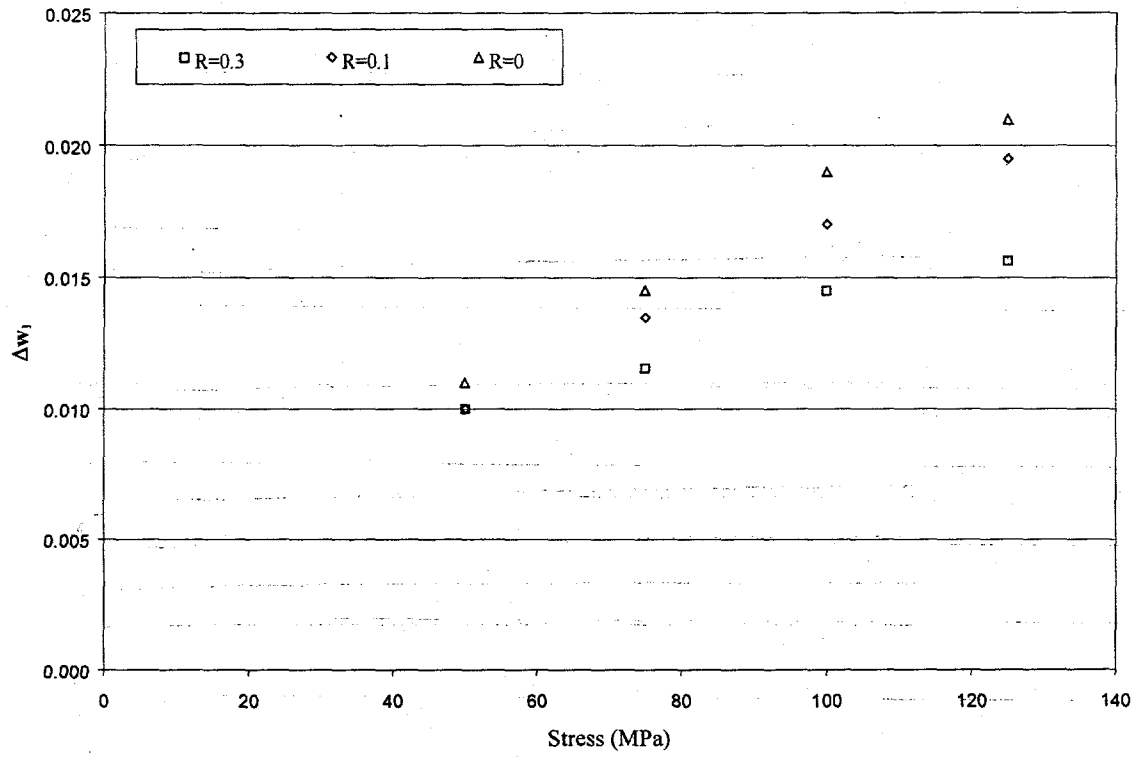
Fig. 34. Damage parameter Δw_1 vs. stress σ.
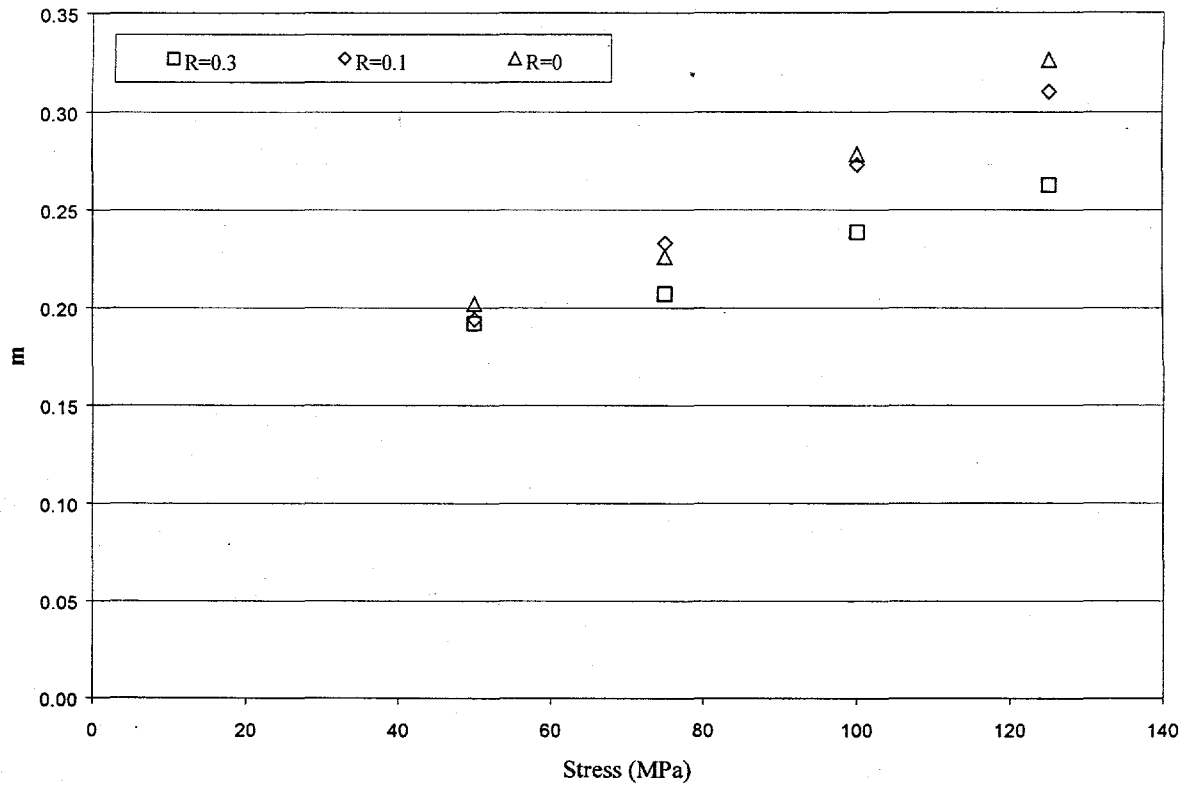
Fig. 35. Damage parameter m vs. stress σ.
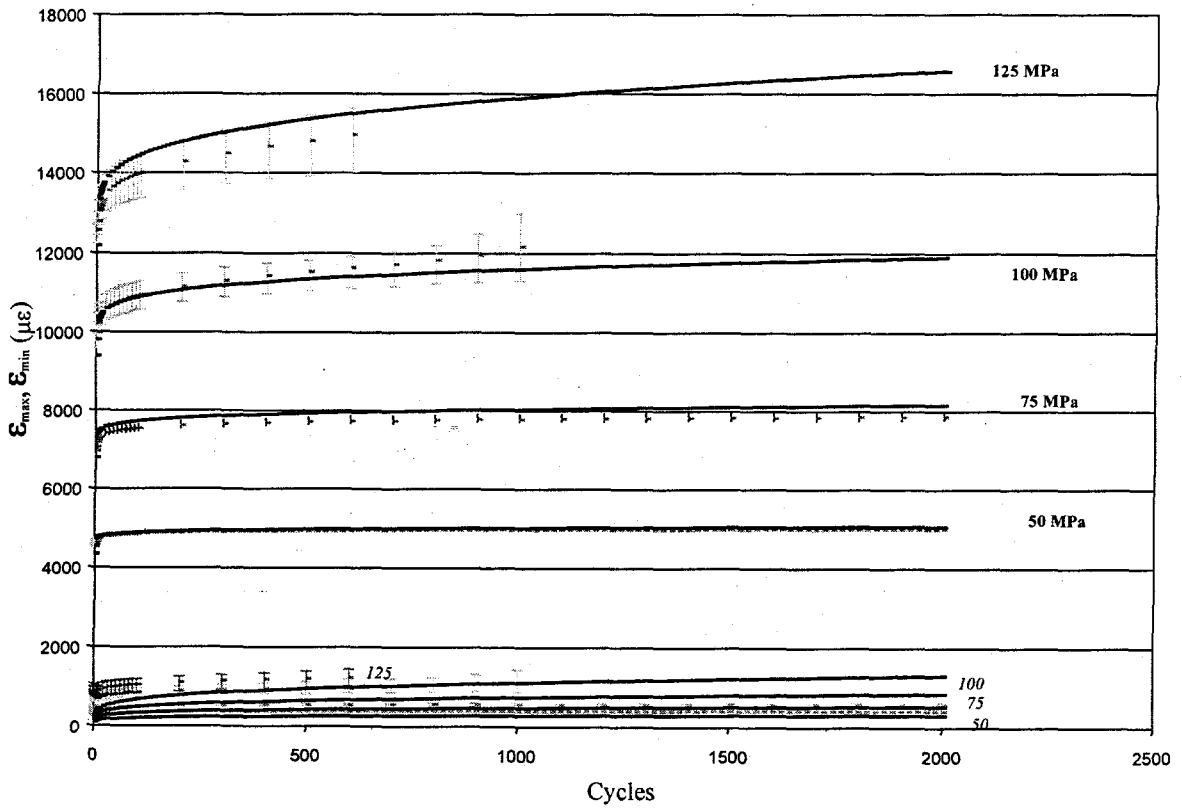
Fig. 36. Scaled measured and predicted strain vs. number of cycles at various levels of maximum stress at R=0. Data (---) with scatter bands, as compared with predictions according to Eqs. (19) and (20) (—). Bold numbers correspond to maximum strains, and plain numbers correspond to minimum strains.
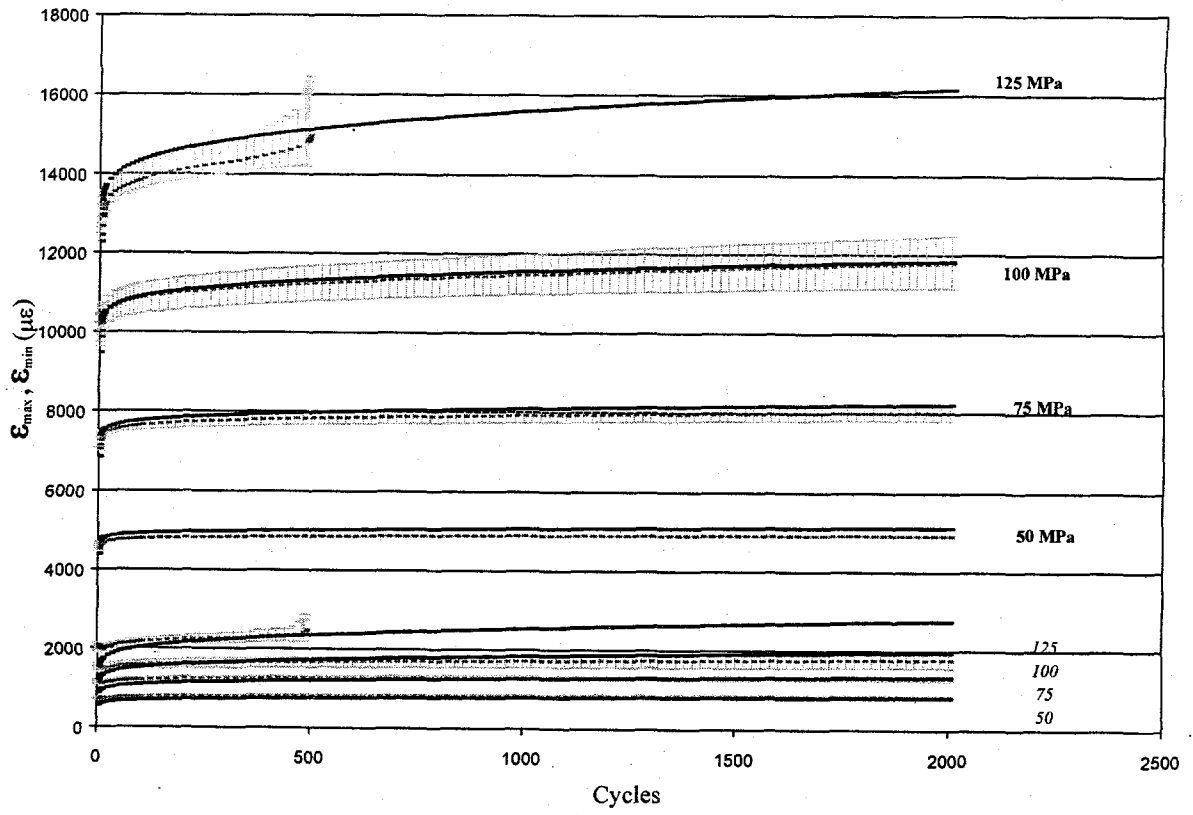
Fig. 37. Same as Fig. 36, but R=0.1.

42
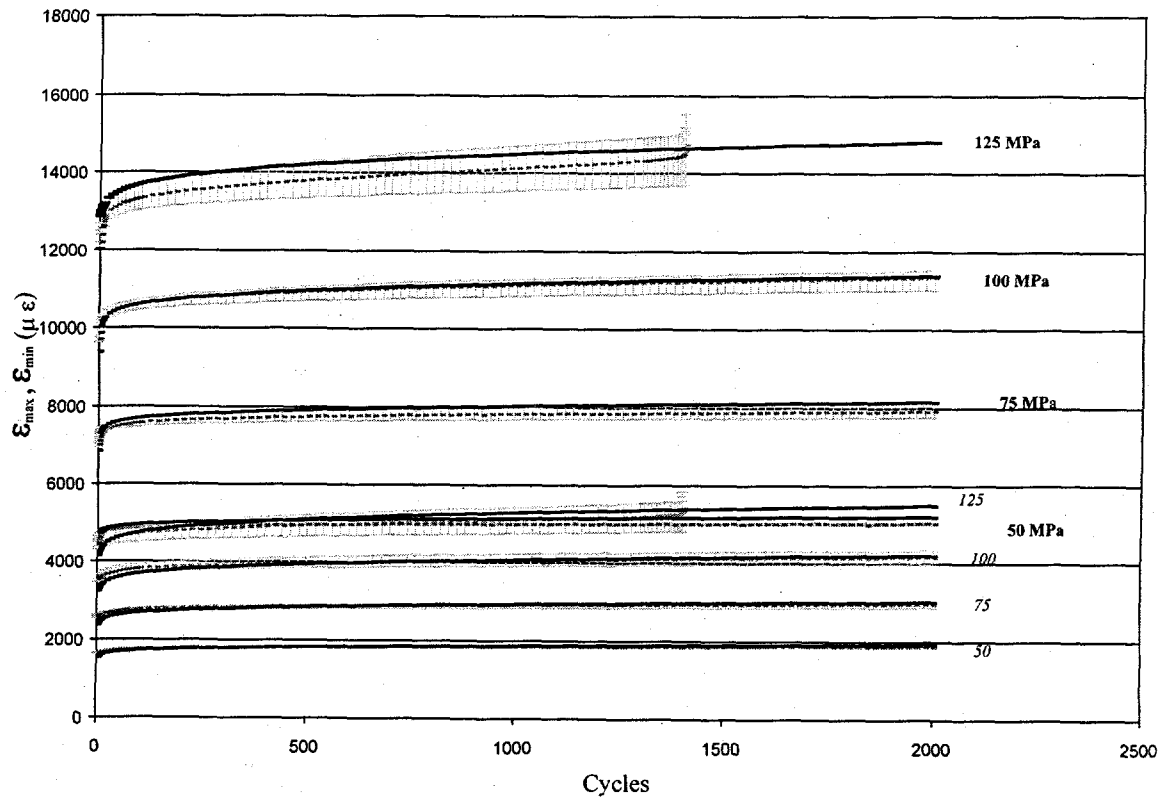
Fig. 38. Same as Fig. 36, but R=0.3.

43
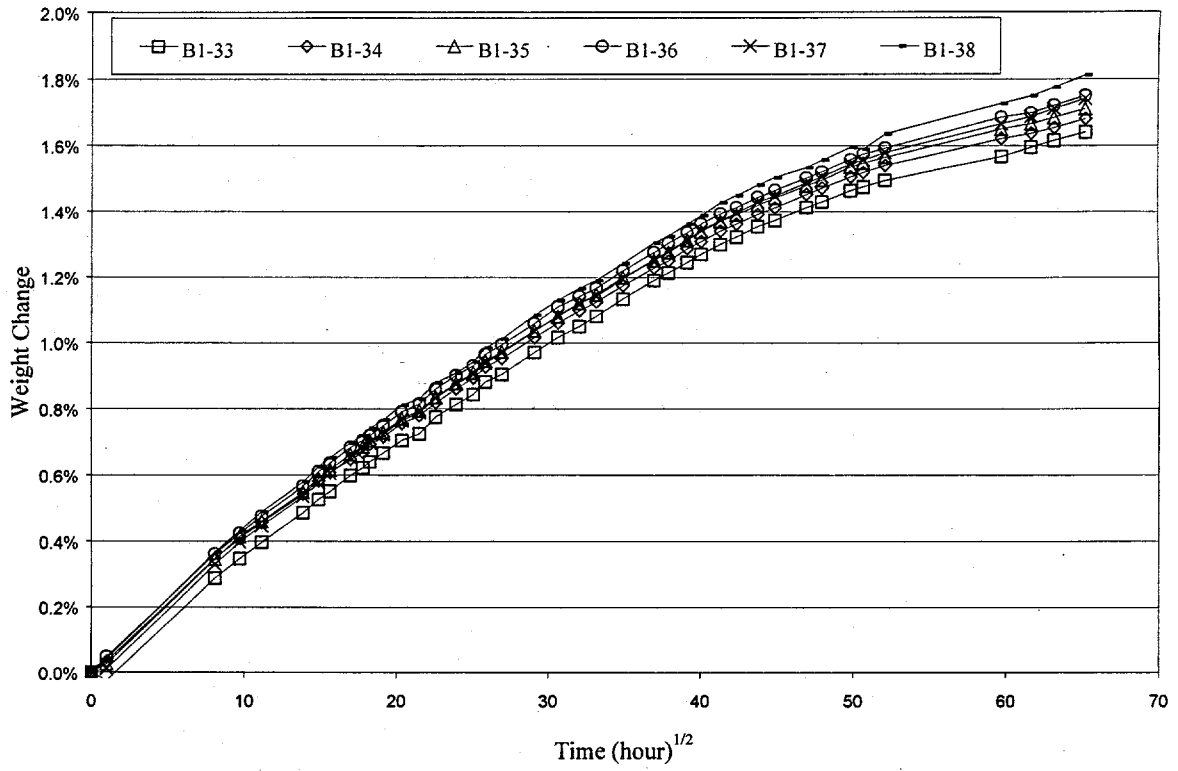
Fig. 39. Weight-gain data (in percent of dry weight) vs. square root of time for P4 chopped glass/urethane composite coupons, immersed in distilled water at temperature T=23 °C. Coupons were not pre-tested in creep prior to immersion.
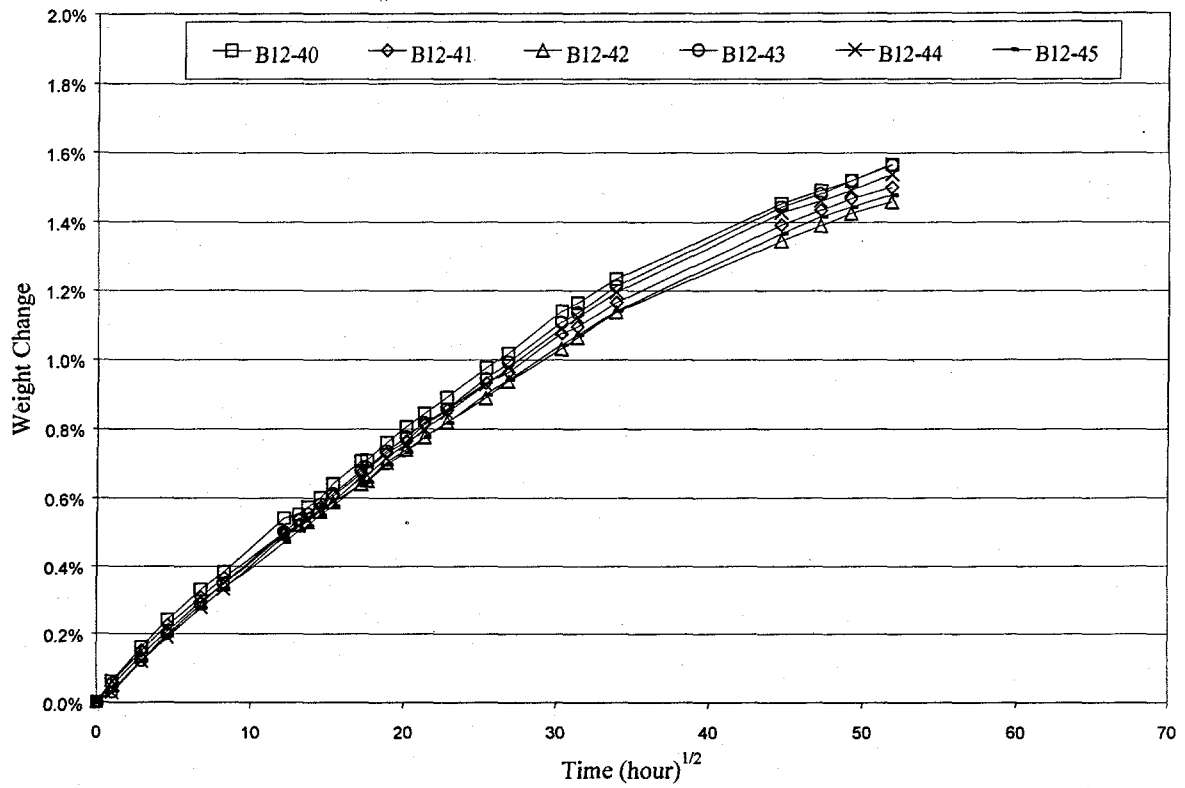
Fig. 40. Weight-gain data (in percent of dry weight) vs. square root of time for P4 chopped glass/urethane composite coupons, immersed in distilled water at temperature T=23 °C. Coupons were pre-tested in creep upon drying and prior to immersion.
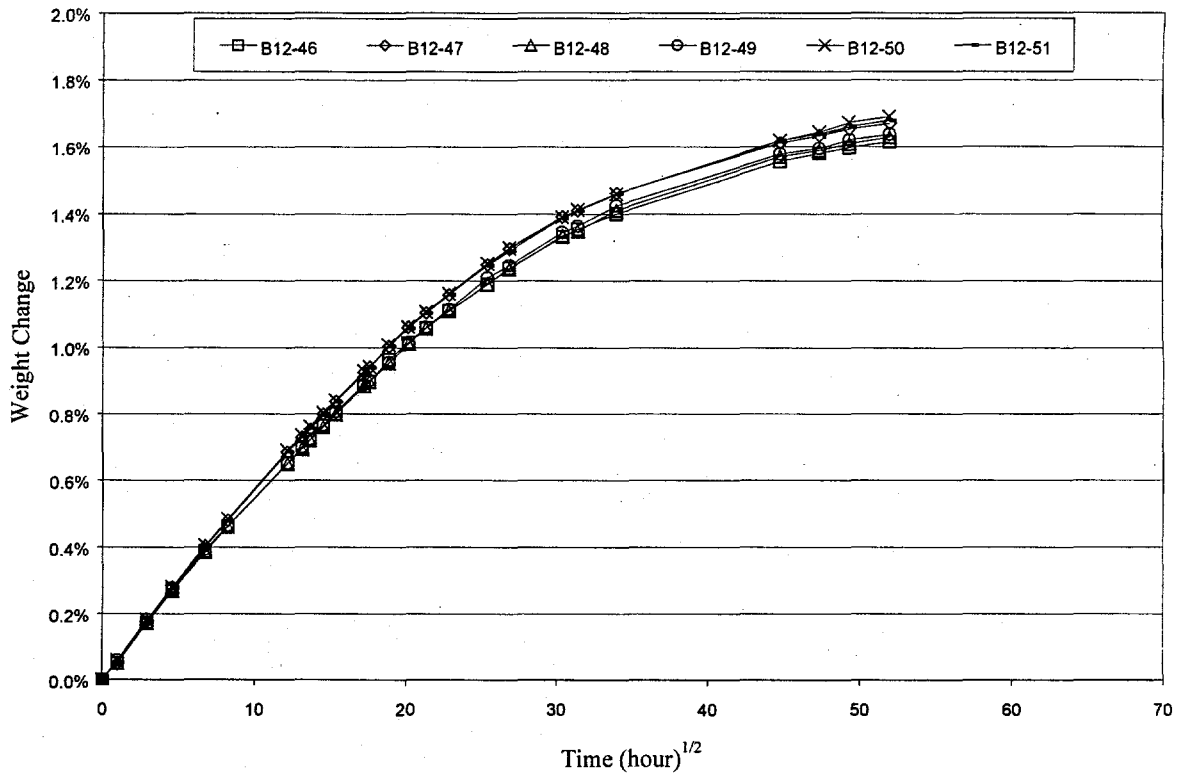
Fig. 41. Same as Fig. 40, but with T=36 °C.
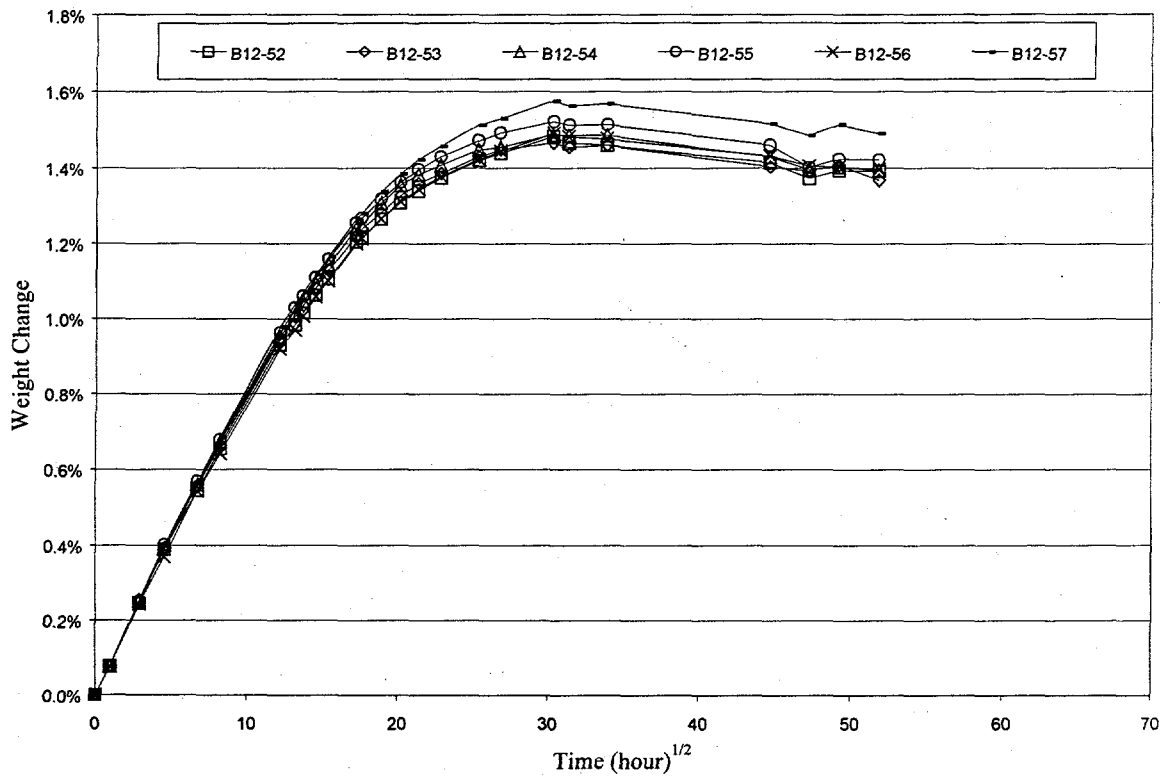
Fig. 42: Same as Fig. 40, but with T=50 °C.
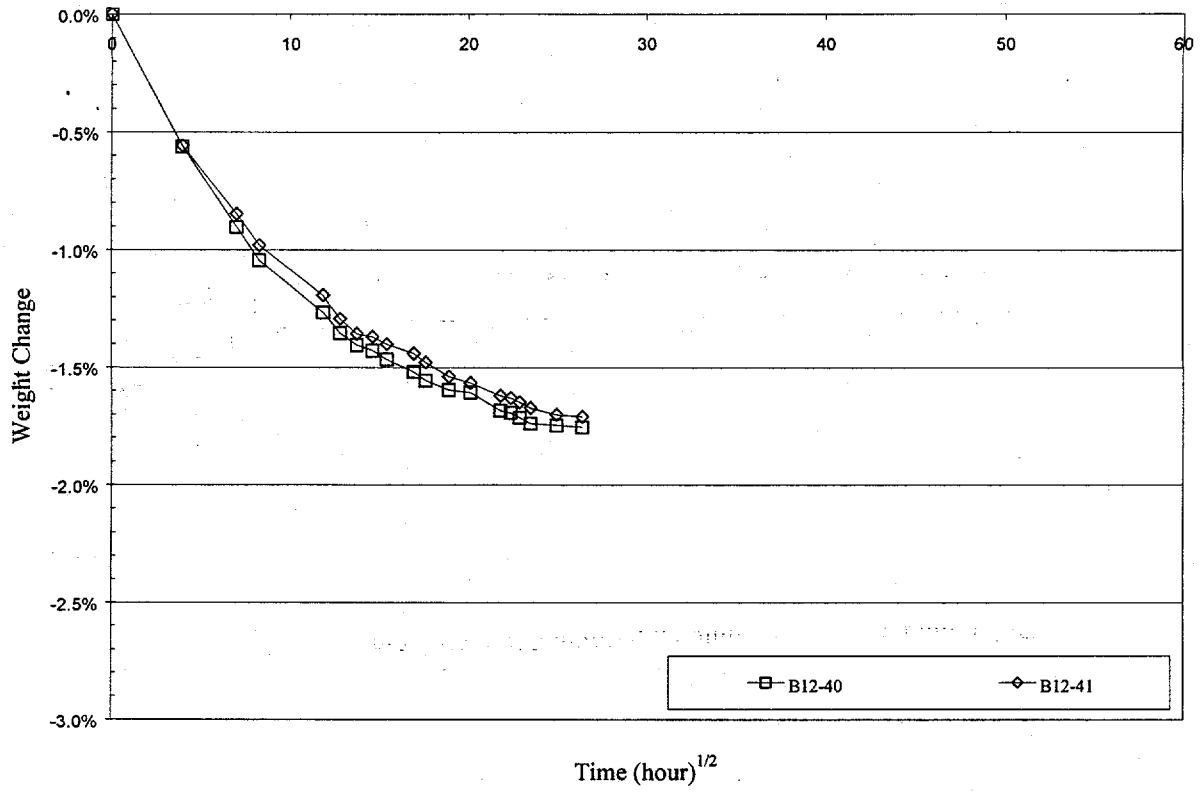
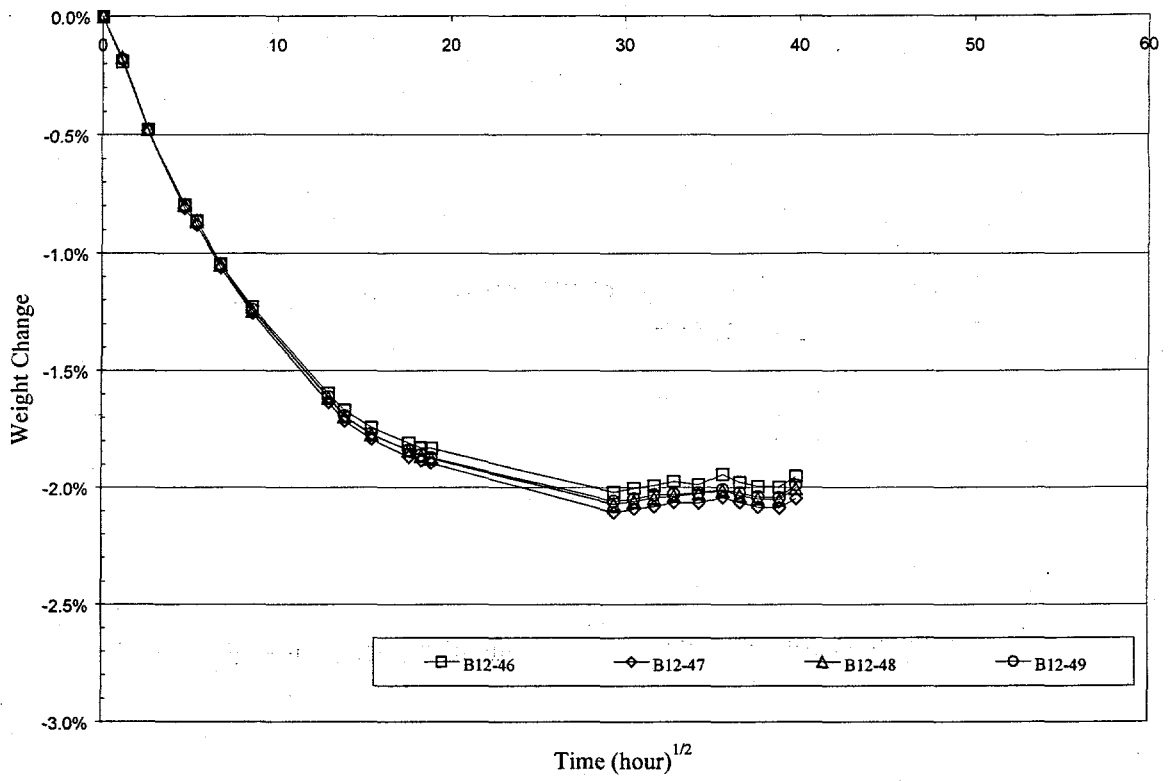**Fig. 43. Weight-loss data (in percent dry weight) upon re-drying of coupons immersed in distilled water at T=23 °C.**

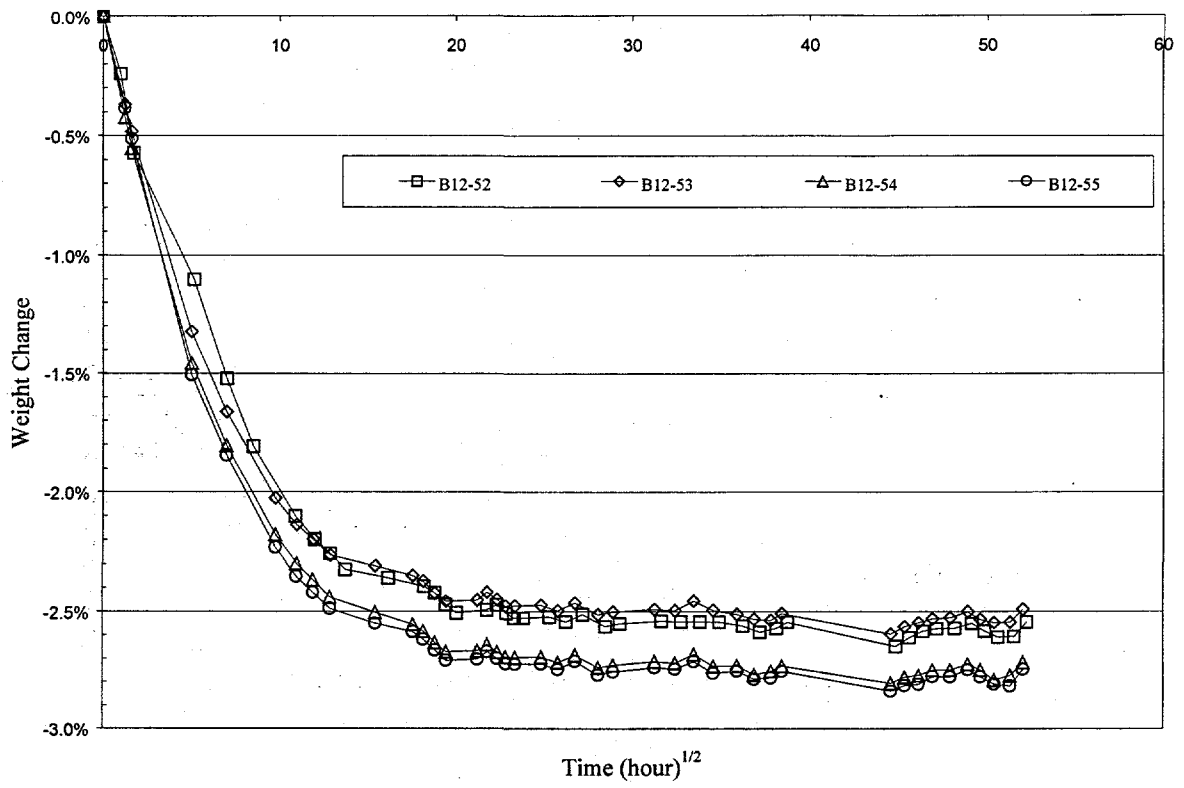**Fig. 44: Same as Fig. 43, but T=36 °C.**
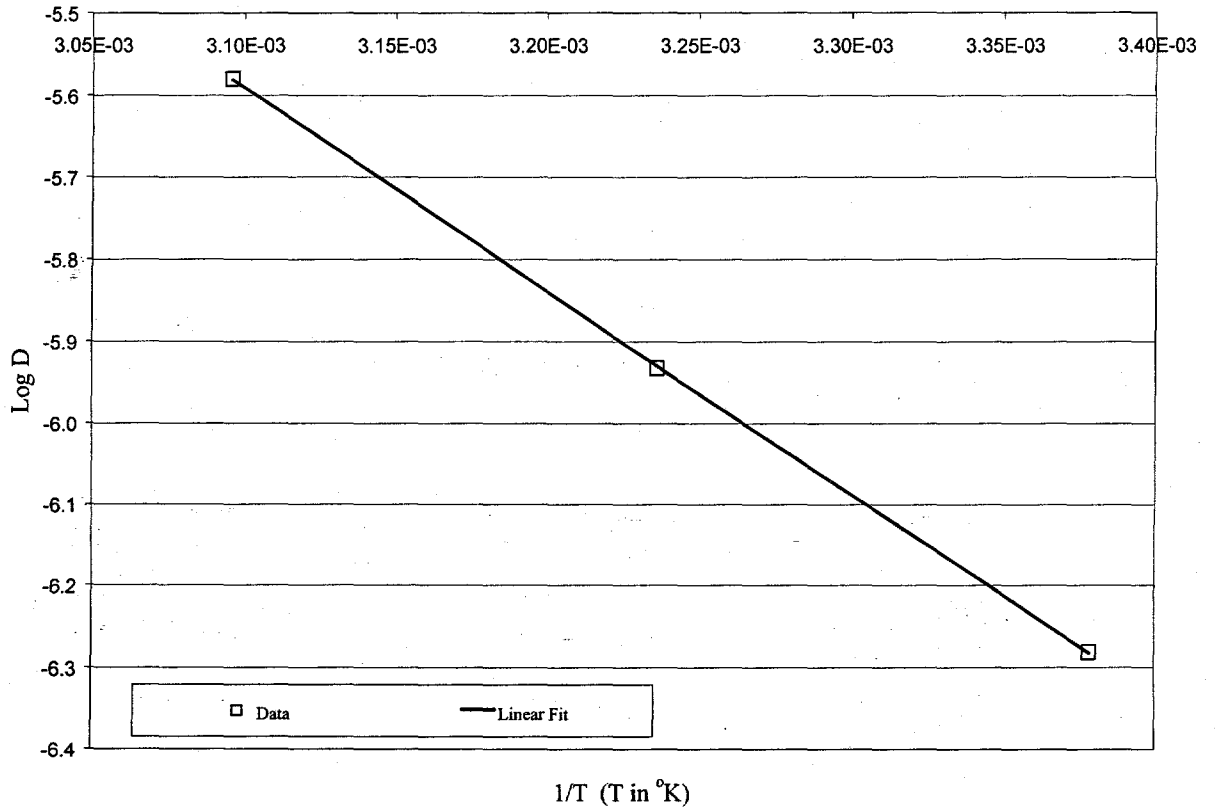
Fig. 45. Same as Fig. 43, but T=50 °C.

Fig. 46. Variation of the diffusion coefficient D with temperature corresponding to data shown in Figs. 40-42.
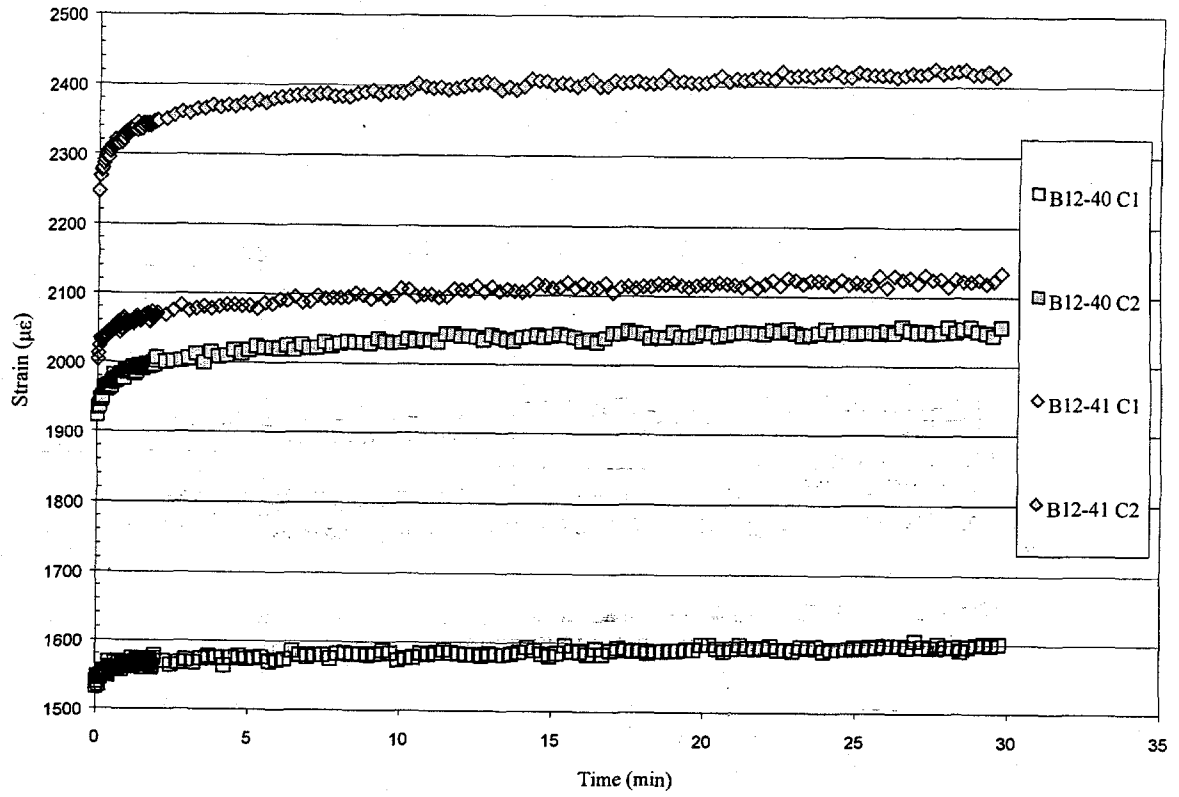
Fig. 47. Comparative data for creep strains of two P4 chopped glass/urethane composite coupons at initially dry state (open symbols) and after saturation in distilled water at T=23 °C (filled symbols). Stress σ=25 MPa, loading duration t_o=30 minutes.
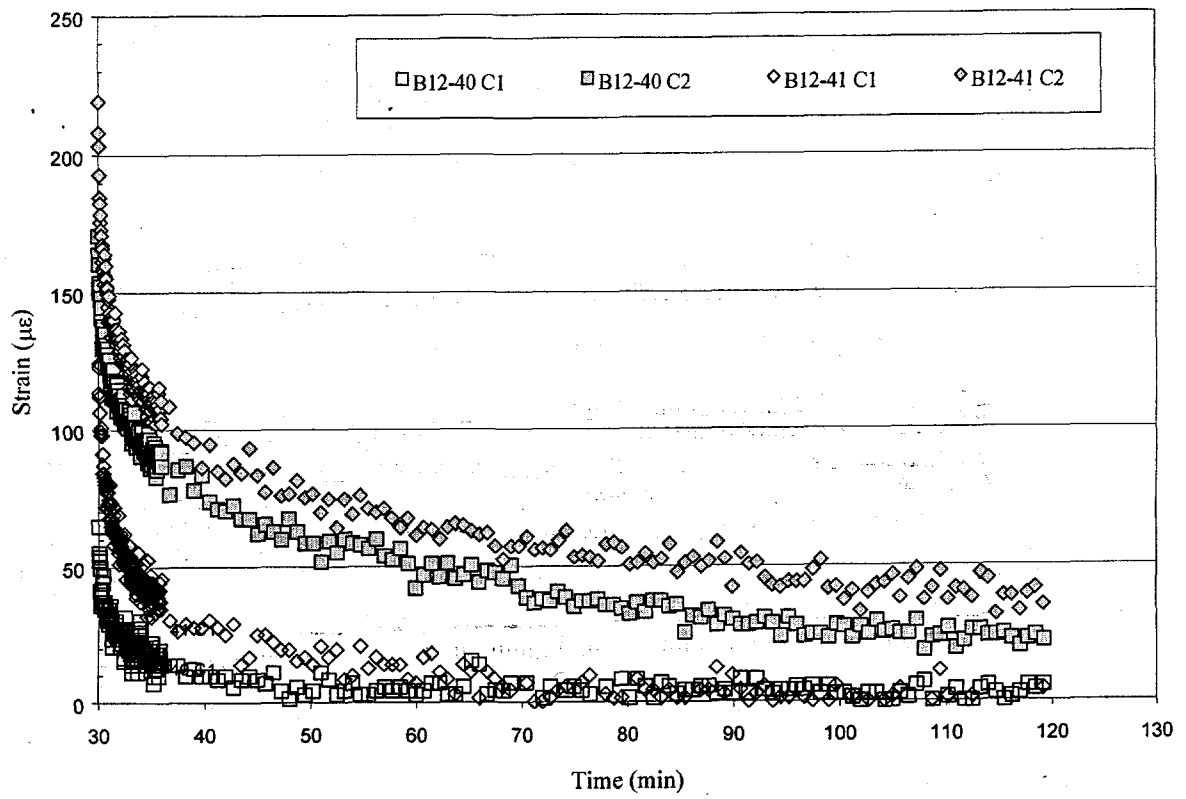
Fig. 48. Comparative data for recovery strains upon load removal at t₀=30 minutes. Exposure conditions and symbols same as in Fig. 47.
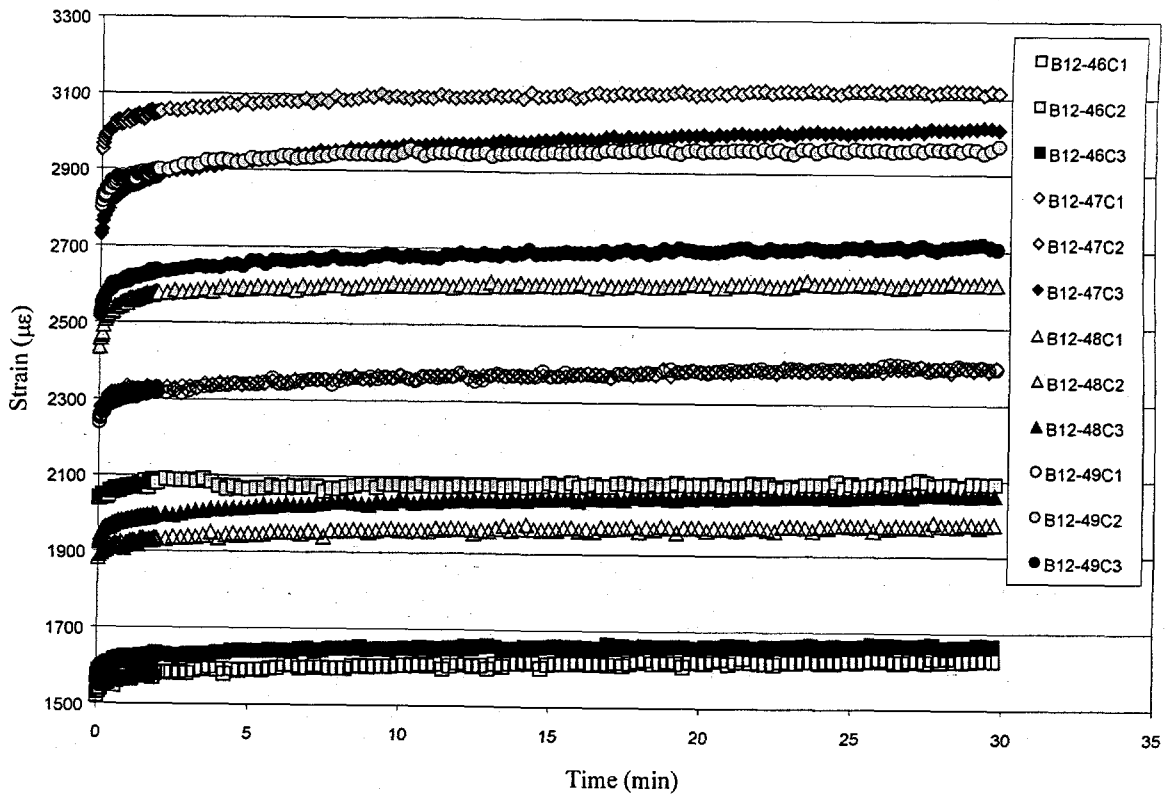
53

Fig. 49. Comparative data for creep strains of four P4 chopped glass/urethane composite coupons at initially dry state (open symbols), after saturation in distilled water at T=36 °C (gray symbols), and after redrying (black symbols). Stress σ=25 MPa, loading duration t_0=30 minutes.
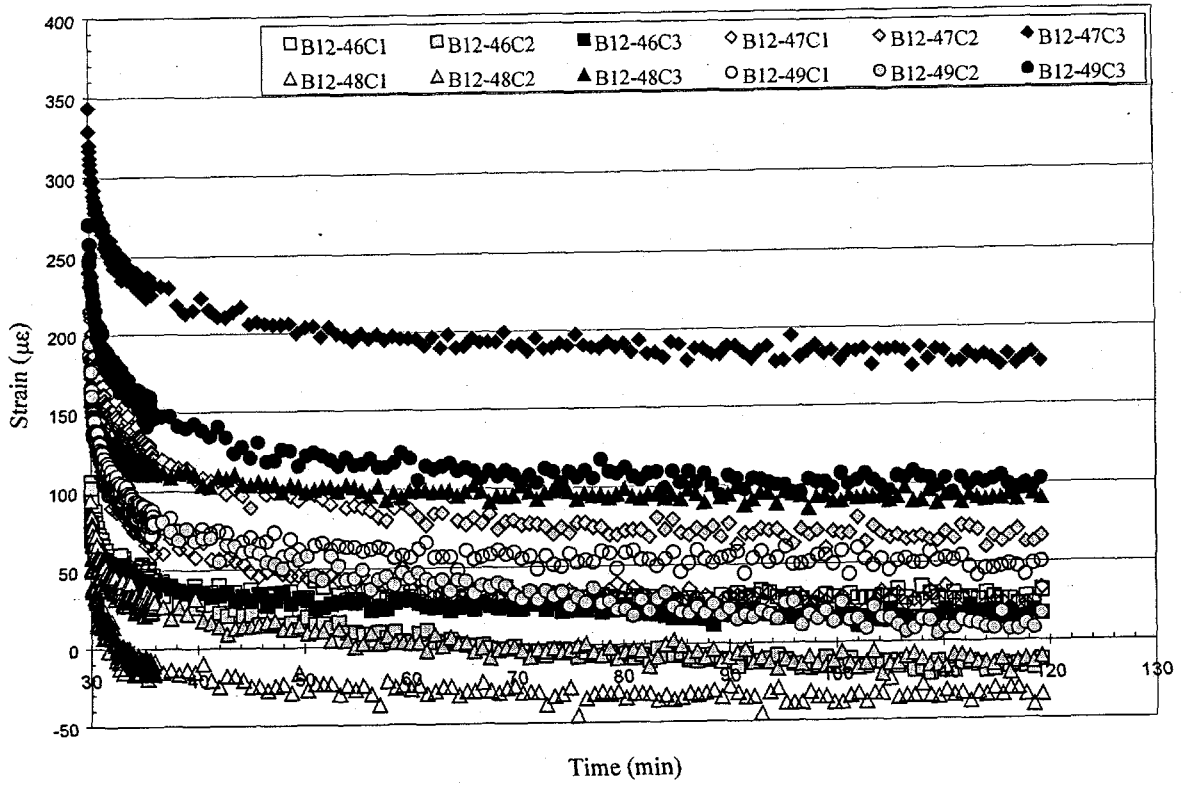
Fig. 50. Comparative data for recovery strains upon load removal at t_0=30 minutes. Exposure conditions and symbols same as Fig. 49.
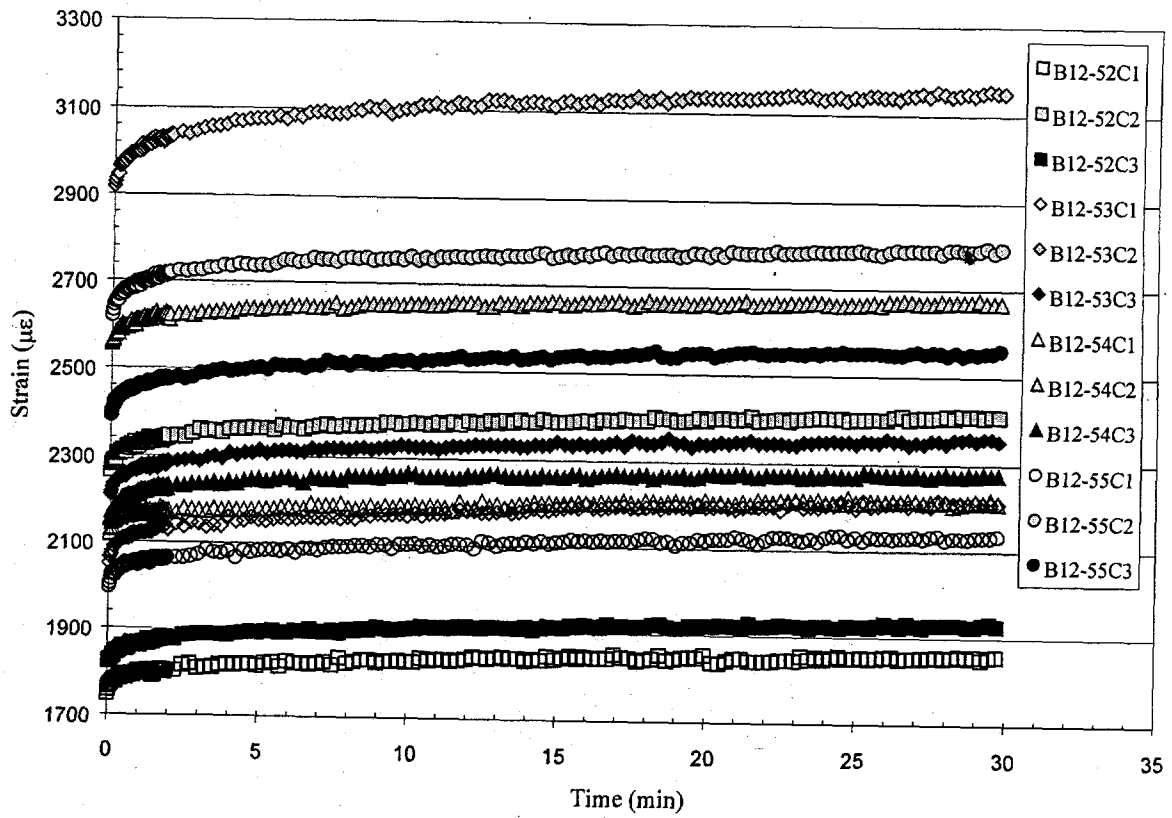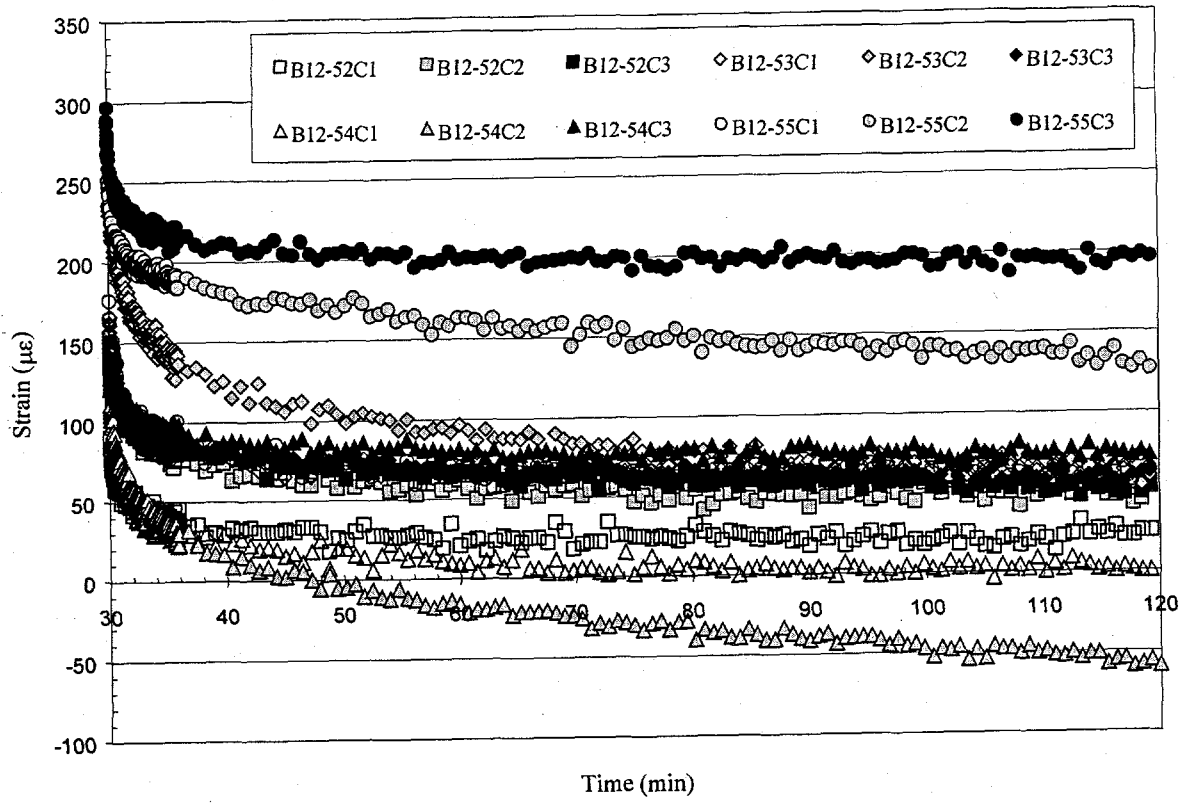
Fig. 51. Same as Fig. 49, but T=50 °C.
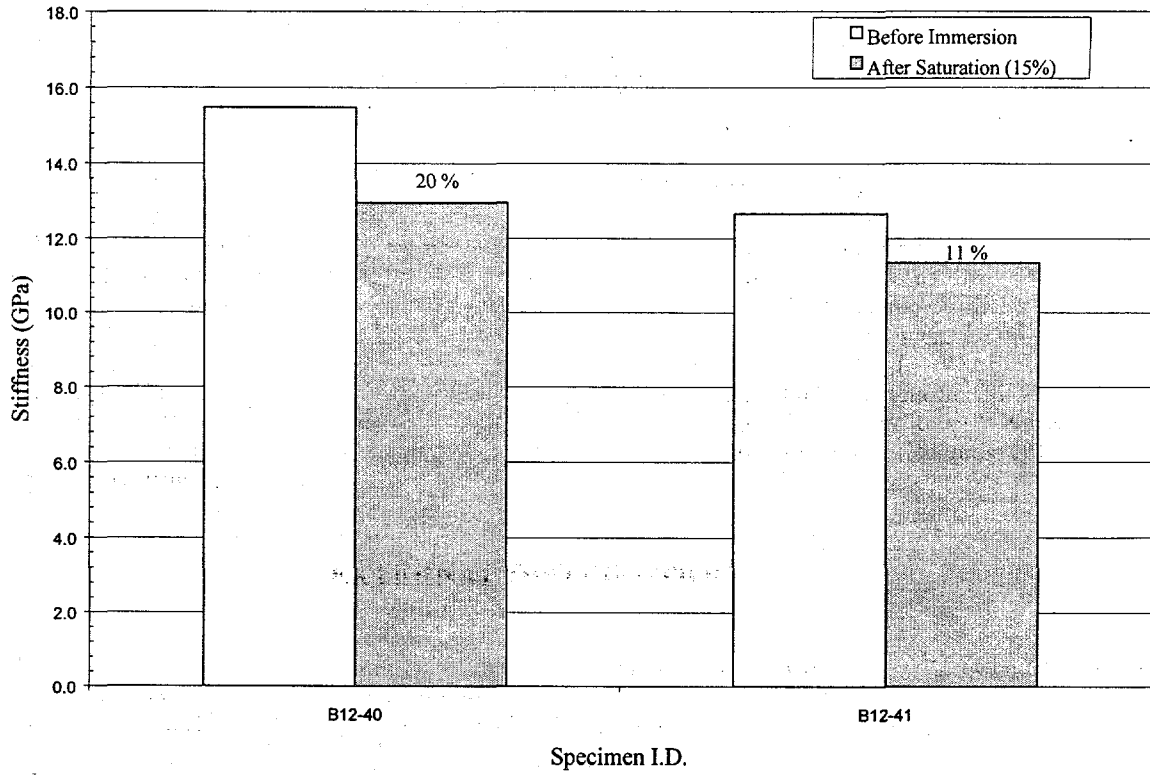
Fig. 52. Same as Fig. 50, but T=50 °C.

Fig. 53. Stiffness degradation of two P4 chopped glass/urethane composite coupons due to immersion in distilled water at T=23 °C.

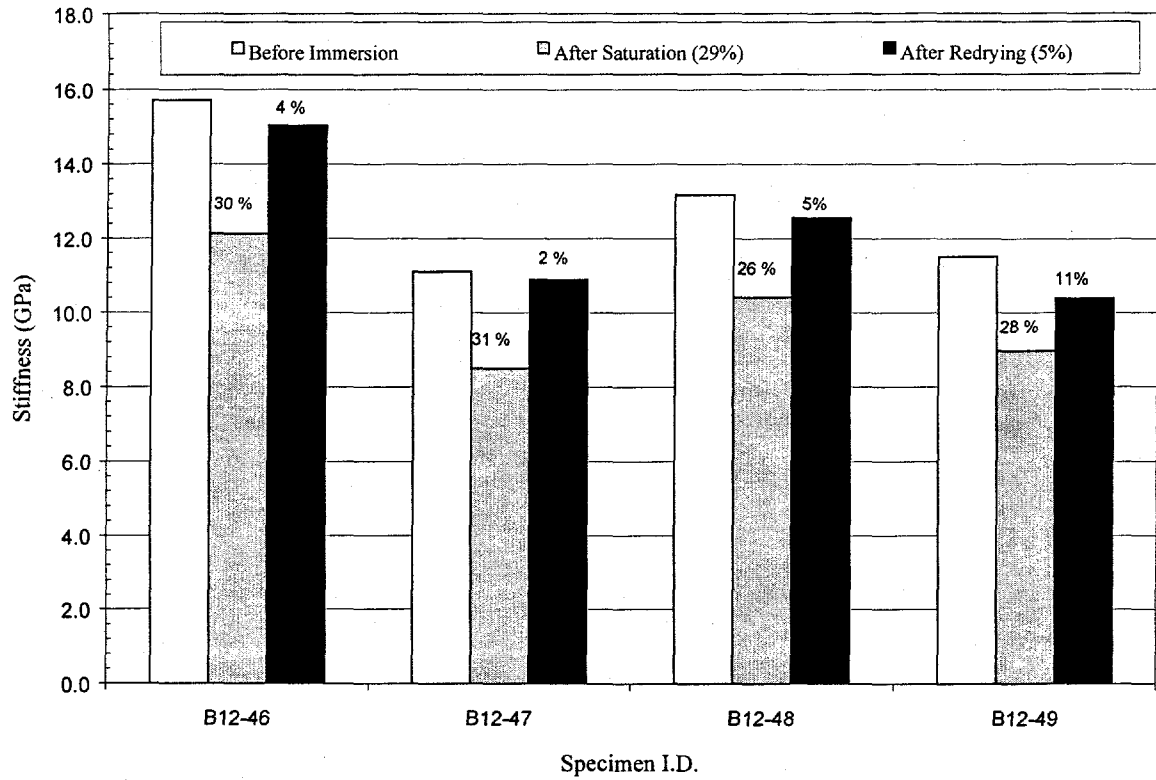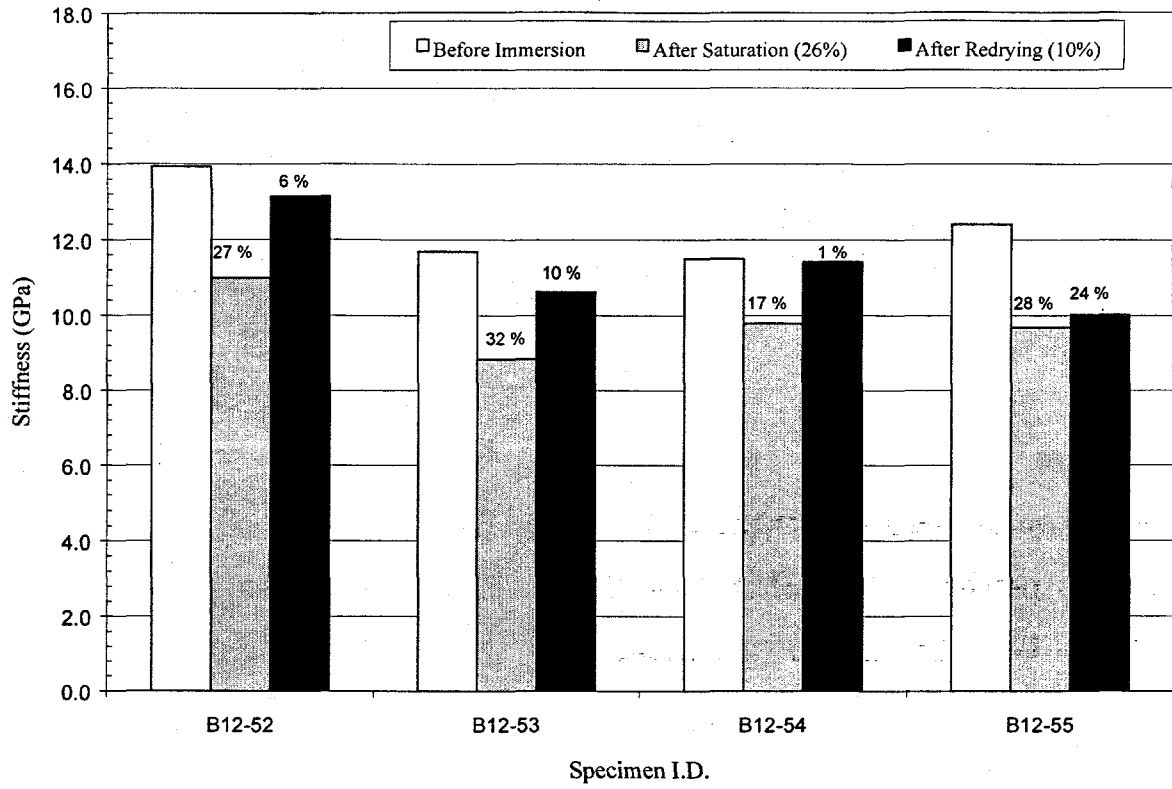**Fig. 54. Same as Fig. 53, but T=36 °C.**

Fig. 55. Same as Fig. 53, but T=50 °C.

INTERNAL DISTRIBUTION

1.	R. L. Battiste	15.	J. M. Starbuck
2.	R. G. Bowman	16.	P. A. Sklad
3.	C. R. Brinkman	17.	C. D. Warren
4–7.	J. M. Corum	18–30.	Y. J. Weitsman
8.	W. G. Craddick	31.	G. T. Yahr
9.	S. Deng	32.	S. Simunovic
10.	D. L. Erdman	33.	R. E. Ziegler
11.	J. G. Hansen	34.	ORNL Patent Section
12.	L. D. Klett	35.	Laboratory Records, ORNL-RC
13.	R. E. Norris	36.	Laboratory Records, OSTI
14.	M. B. Ruggles		

EXTERNAL DISTRIBUTION

37–65. E. M. Hagerman, Automotive Composite Consortium, General Motors, 30500 Mound Road, I-6, Box 9055, Warren, Michigan 48090-9055.

66. J. M. Henshaw, Department of Mechanical Engineering, The University of Tulsa, 600 S. College Avenue, Tulsa, Oklahoma 74104-3189.

67. G. A. Holmes, National Institute of Standards and Technology, Bldg. 224, Room B116, MS: Room B108, Gaithersburg, Maryland 20899.

68. K. Liechti, Engineering Mechanics Research Laboratory, Department of Aerospace Engineering and Engineering Mechanics, The University of Texas at Austin, Austin, Texas 78712.

69. D. Oplinger, AAR-431, FAA William J. Hughes Technical Center, Atlantic City International Airport, New Jersey 08405.

70. T. A. Reinhart, The University of Dayton Research Institute, 300 College Park Drive, Dayton, Ohio 45469-0130.

71. W. Ren, AFRL/MLLN, 2230 Tenth St., Bldg. 655, Rm. 23, WPAFB, OH 45433-7817.

72. G. Sandgren, Owens Corning Science & Technology Centre, 2790 Columbus Road, Route 16, Granville, Ohio 43023-1200.

73. R. A. Schapery, Engineering Mechanics Research Laboratory, Department of Aerospace Engineering and Engineering Mechanics, The University of Texas at Austin, Austin, Texas 78712.

74. C. R. Schultheisg, National Institute of Standards and Technology, Building 224, Room A209, Gaithersburg, Maryland 20899.

75. T. D. Seagrave, Bayer Corporation, 100 Bayer Road, Pittsburgh, Pennsylvania 15205.

76. L. V. Smith, Washington State University, School of Mechanics and Materials Engineering, Pullman, Washington 99164-2920.

76–80. J. A. Carpenter, U.S. Department of Energy, 1000 Independence Avenue, SW, Washington, DC 20588.

81. P. G. Patil, U.S. Department of Energy, 1000 Independence Avenue, SW, Washington, DC 20588.

82. M. Rowlins, U.S. Department of Energy, Oak Ridge Site Office, Oak Ridge, Tennessee 37831.